

The Landscape of Subcellular Long Non-coding RNAs Links Organelle Metabolic Homeostasis

Ling-jie Sang

Zhejiang University

Huai-Qiang Ju

Sun Yat-sen University Cancer Center <https://orcid.org/0000-0003-1713-5465>

Zuo-zhen Yang

Zhejiang University

Qi-wei Ge

Zhejiang University <https://orcid.org/0000-0003-1689-6836>

Zhen Zhang

Zhejiang University

Fang-zhou Liu

Zhejiang University

Luo-jia Yang

Zhejiang University

Hang-di Gong

Zhejiang University

Chengyu Shi

Zhejiang University

Lei Qu

Zhejiang University

Hui Chen

Zhejiang University

Min-jie Wu

Zhejiang University

Hao Chen

Zhejiang University

Rui-hua Li

Zhejiang University

Qian-qian Zhuang

Zhejiang University

Hai-long Piao

Chinese Academy of Sciences

Qingfeng Yan

College of Life Science, Zhejiang University <https://orcid.org/0000-0002-5381-8426>

Weishi Yu

Cipher Gene LLC

Liang-jing Wang

Zhejiang University

Jianzhong Shao

Zhejiang University

Jian Liu

Zhejiang University

Wenqi Wang

University of California, Irvine

Tianhua Zhou

Zhejiang University

Aifu Lin (✉ linaifu@zju.edu.cn)

Zhejiang University

Article

Keywords: Subcellular lncRNAs, organelles, metabolic homeostasis, TCA cycle

Posted Date: September 16th, 2020

DOI: <https://doi.org/10.21203/rs.3.rs-78018/v1>

License:  This work is licensed under a Creative Commons Attribution 4.0 International License.

[Read Full License](#)

Abstract

Organelles entail specialized molecules to regulate their essential cellular processes. However, systematically elucidating the subcellular distribution of functional molecules such as long non-coding RNAs (lncRNAs) in tissue homeostasis and diseases has not been fully achieved. Here, we characterized the organelle-associated lncRNAs from mitochondria, lysosome, and endoplasmic reticulum (ER), respectively, and revealed the diverse and abundant distribution of lncRNAs. Among them, we identified mitochondrial lncRNA Growth-Arrest-Specific 5 (GAS5) as a tumor suppressor in maintaining cellular energy homeostasis. Mechanistically, energy stress-induced GAS5 modulated mitochondria TCA flux by declining metabolic tandem association of FH-MDH2-CS, the canonical members of the TCA cycle. Remarkably, the expression of GAS5 negatively related with levels of its associated mitochondrial metabolic enzymes and breast cancer development. Together with the detailed functional annotations, this subcellular lncRNA identification revealed the human cell's inquisitively complex architecture, aiding in the development of new strategies for the clinical application of organelle-associated lncRNAs.

Introduction

Organelles are microscopic semi-organs that underlie many cellular processes, including several important metabolic reactions, energy production, cellular signaling, and cell growth¹⁻⁶. Each organelle, such as mitochondrion, lysosome, and endoplasmic reticulum (ER) carries out its faithfully characteristic functions as it possesses a unique set of proteins, lipids, and other molecular factors⁷⁻¹⁰. Multiple unique roles of organelles are revealed through searching the hierarchical dynamics of compartmentalized pools of molecules. For example, analyzing lysosome proteomics and metabolomics revealed its critical roles in regulating metabolic resource sensing and allocation^{11,12}. Quantitative proteomics analysis of mitochondria Acylomes identified it as the holder of Acylomes¹³. It showed that it regulated the TCA cycle highly through the acylation of the critical targets (*e.g.*, MDH2)¹³. Therefore, comprehensively exploring and defining such organelle-possessed unique molecular sets aid in unveiling the *de novo* functions of organelles, which provides novel insights into their associated cellular functions in human diseases like cancer.

Accumulating evidences have indicated that extensive lncRNAs are located in the cytosol and involved in multiple signaling pathways in homeostasis and human diseases¹⁴⁻¹⁷. Our recent study also showed that lncRNAs were naturally associated with the lipid components of the cellular membrane and played critical roles in signaling pathways¹⁴. This finding suggested that the localization of lncRNAs played a vital role in implementing their functions in various cellular processes. Decoding the subcellular distribution of organelle-associated lncRNAs will provide an important resource to interpret the complex subcellular architecture, cell dysfunction, and pathophysiology of human diseases.

Although the cytoplasmic RNAs are presumably thought to function in a wide range of organelle-associated biological processes, the understanding of subcellular RNAs is still limited. Most of the current techniques for detecting subcellular localization of RNAs follow the image-observing and fraction-

sequencing methods. RNA fluorescence tracking methods show limitations when it comes to deeply high-throughput screening¹⁸⁻²⁰. Traditional fraction-sequencing ways are more suitable for subcellular RNA set identification. However, the distinguishability and fidelity of centrifugation fraction-based approaches are plagued by intricate contamination²¹.

Here, we developed a new strategy to obtain the bona fide subcellular components by coupling centrifugation with an endogenous immunoprecipitation approach. Through it, we isolated mitochondria, lysosome, and ER, followed by RNA-sequencing. This work achieved a full characterization of the organelle-associated RNAs. We next validated the top candidates and confirmed their critical roles in diverse cellular functions. Among them, we focused on the role of a mitochondria-associated lncRNA *Growth-Arrest-Specific 5 (GAS5)*. We found that *GAS5* was highly sensitive to the energy condition and functioned as a critical regulator in mitochondria metabolism and cell growth. Previous studies showed that *GAS5* acted as a DNA decoy for glucocorticoid receptor (GR) to respond to growth factors²², regulated insulin receptor (*INSR*) gene transcription in adipocytes²³, and functioned as an RNA sponger to buffer miRNAs²⁴. However, these findings were mostly limited in investigating the specific sensitivity of *GAS5* to glucose and its dynamic spatial manner. Strikingly, our results suggested that *GAS5* blocked the FH-MDH2-CS metabolic tandem association by decreasing the MDH2 acetylation and eventually reduced mitochondrial TCA flux. Remarkably, high expression of *GAS5* and low TCA flux benefited clinical outcomes in breast cancer patients. Therefore, our findings provided a potentially robust biomarker for cancer, offering more valuable future investigation targets.

Results

Purification and validation of intact organelle components

We applied an improved organelle isolation method to isolate the bona fide organelle components by combining the standard density centrifugation with immunoprecipitation to obtain the non-artificial subcellular fractionations in HEK293T live cells (**Fig. 1a**). This method allowed us to isolate organelle components with unwavering confidence and investigate their subcellular reactions under different signaling contexts. We first attained the crude light mitochondria fraction (LMF), which mainly contained mitochondria and lysosome fraction according to the classical organelle fraction guide's sedimentation effect. We then used specific antibodies coupled with protein A/G magnetic beads to immunoprecipitate the antigen-anchored organelles. Moreover, we conducted the sucrose density centrifugation to isolate the ER (**Fig. 1a**). The purified organelle components were further confirmed using their resident protein markers: mitochondria (i.e., Tom20), lysosome (i.e., LAMP2), ER (i.e., Calnexin), cytosol (i.e., GAPDH), and nucleus (i.e., Lamin B) (**Fig. 1b**). The integrity of the isolated subcellular components was also verified through fluorescence sharp granular sensation of the isolated organelles (**Extended Data Fig. 1a-c**). The ribosome translated canonical secreted proteins and plasma membrane-harbored proteins on the surface of rough ER²⁵. Their corresponding mRNAs (e.g., *FGF2* and *TJP1*) were thereby supposed to enrich in the ER fraction. Many mRNAs' subcellular distributions were concordant with their coding proteins' spatial

localization^{26,27}. Thus, we chose the lysosomal Lamp2 protein's coding mRNA as the marker for the lysosome RNA set. We validated the mitochondria, lysosome, ER sets by the other organelles-specific markers (including protein and RNA levels), which helped exclude the organelle cross-contaminants. The relative enrichment of each RNA was calculated by $2^{-(Ct_{Mito}-Ct_{Total})}$ followed by normalizing all ratio value to the *GAPDH* in the control group (Value of the first *GAPDH* column was normalized as 1), and the value of the cut-off line was determined as 1. The relative RNA enrichment of marker genes in each indicated organelle further confirmed the purity of isolation fractions (**Fig. 1c**). Notably, clear isolation between lysosome and mitochondria was difficult when using classical centrifugation-based organelles fraction methods because of their very similar sedimentation effect. However, we found little cross-contamination in isolated mitochondria and lysosome fraction (**Fig. 1b, c**), which attested the ability of this isolation method to distinguish the different subcellular RNAs among organelles.

Overview of the organelle-associated RNAs

To explore the subcellular organelle-associated lncRNAs, we sequenced ten samples from five groups (i.e., total RNAs, LMF, mitochondria, lysosome, and endoplasmic reticulum) in HEK293T cells. Quality control analyses, including individual expression distribution, technical replicates' assessment, and principal component assays, were applied to attest these sequence results ($R > 0.95$, $P < 0.05$) (**Fig. 1d-i**, **Extended Data Fig. 1d-f** and **Supplementary Table 1**), suggesting the consistency of the replicates within each group. Our sequence results utilizing the DESeq2 method²⁸ suggested the enrichment of organelle-associated RNA markers (highlighted in red) was enriched better than LMF fractionation (**Fig. 1e, f**). Through it, we revealed 2292 organelle-associated lncRNAs (Organelle/Total, $P < 0.05$, fold-change > 1.5 for enrichment threshold) (**Supplementary Table 1**), which covered 5.2% of all the detected total lncRNAs in HEK293T cells (**Fig. 1g**). Moreover, we characterized both the unique and overlapping distribution patterns of the organelle-associated lncRNAs and mRNAs, respectively (**Fig. 1d, h, i** and **Extended Data Fig. 1g, h**). Through it, 370 lncRNAs were identified in all three organelles (i.e., mitochondria, lysosome, and endoplasmic reticulum) (**Fig. 1h**). Further lncRNA expression enrichment and cluster heatmap assays confirmed the specificity and diversity of the organelle-associated lncRNAs (**Fig. 1j**). As expected, the known nuclear-located lncRNA genes (*NEAT1*, *XIST*) were not enriched in the indicated organelles, underscoring the purity of our cytoplasmic fraction (**Fig. 1j**). Furthermore, using the organelle-associated specific markers confirmed the constant validation of individual organelle components in our analysis (**Extended Data Fig. 1i**). In summary, our purification strategy showed its merit in specific enriching organelle-associated lncRNAs.

Next, we analyzed the potential function of each organelle-associated lncRNA set using GO and KEGG pathway analyses. We found that each organelle lncRNA set was involved in different GO terms or pathways consistent with their associated organelles (**Fig. 1k** and **Extended Data Fig. 1j-l**). For example, the lncRNAs in the mitochondrial set were found involved in cellular metabolic processes through various metabolism-related signaling events, such as AMPK signaling, alcoholism, and TNF signaling pathways (**Extended Data Fig. 1j-l**).

Functional validation of subcellular lncRNAs in cellular homeostasis

We validated the subcellular lncRNAs distribution and potential functions accompanied by their associated organelles. A high abundance of organelle lncRNA component enrichment was observed by picking up the lncRNA candidates of each set for the RT-qPCR validation. Among them, we respectively confirmed 21 out of 23 mitochondrial lncRNAs (**Extended Data Fig. 2a**), 10 out of 15 lysosome lncRNAs (**Extended Data Fig. 2b**), and 3 out of 14 ER lncRNAs (**Extended Data Fig. 2c**) for each isolated organelle. Through siRNA screening (**Extended Data Fig. 2d, e**), the subcellular lncRNAs were strikingly characterized functions in many important cellular processes (e.g., Glucose sensitivity and ATP production), which were consistent with their organelle-associated functions (**Fig. 1l, m and Extended Data Fig. 2d-g**). Interestingly, 2 out of 9 lysosome-associated lncRNAs candidates were involved in pivotal cellular energy sensor pathways such as the AMPK pathway (**Fig. 1l and Extended Data Fig. 2d, f**), which was explicitly activated on the surface of the lysosome^{6,10}. Meanwhile, 4 out of 12 mitochondria-associated lncRNAs candidates were involved in mitochondrial ATP generation (**Fig. 1m**), and 9 out of 12 candidates were involved in whole-cell ATP production (**Extended Data Fig. 2e, g**), which was known as an essential function of mitochondria in energy homeostasis. Intriguingly, abundant subcellular lncRNAs could respond to the cellular energy stress condition (**Fig. 1l, m, and Extended Data Fig. 2f, g**), highlighting their potential functions in cellular energy homeostasis. Thus, mapping the subcellular lncRNAs distribution and their pivotal functions further sparked the novel non-canonical molecular mechanisms of organelles through their accompanying components.

Mitochondrial lncRNA *GAS5* is identified as a glucose responder.

Organelles are involved in pivotal metabolic processes, where mitochondria acted as a nexus engine in cellular energy sensing and homeostasis^{1,29}. Among the characterized mitochondrial lncRNAs candidates, *GAS5* was identified as a mitochondria-located and functionally-related lncRNA (**Fig. 1m**). The partial colocalization between *GAS5* and mitochondria was observed either by RNA fluorescence *in situ* hybridization (FISH) or by RT-qPCR (**Fig. 2a-c**), suggesting its potential role in mitochondria-related cellular processes. We also excluded the lysosome and ER distribution of *GAS5*, indicating its unique association with mitochondria (**Extended Data Fig. 3a, b**).

Next, we assessed the function of *GAS5* in responding to cellular energy availability and regulating mitochondrial metabolism. Interestingly, the *GAS5* expression and its association with mitochondria were remarkably increased under glucose-deprivation (**Fig. 2c-e and Extended Data Fig. 3c**). The glucose starvation-caused upregulation of *GAS5* was reversed by glucose restoration (**Fig. 2f**). However, *GAS5* showed less sensitivity to serum starvation, suggesting its specific response to central carbon metabolism (**Extended Data Fig. 3d**). Our data further showed that *GAS5* knockdown promoted oxygen consumption rate (OCR) (**Extended Data Fig. 3e, f**), ATP production (**Fig. 2g, h**), and NADH generation (**Fig. 2i, j**), especially under glucose starvation condition (**Extended Data Fig. 3g, h**). It indicated a crucial role of *GAS5* in mitochondria metabolic regulation.

The *GAS5*-Loop2 region dictates its mitochondrial translocation and function.

To identify *GAS5*-associated proteins potentially involved in the *GAS5*-related mitochondrial regulation, we performed an RNA pulldown assay followed by mass spectrometry (MS) analysis^{15,30} (**Fig. 2k, Extended Data Fig. 3i and Supplementary Table 2**). Interestingly, the sense *GAS5*, rather than the antisense or beads control, bound to MDH2, a canonical member of the mitochondrial TCA cycle as well as a mitochondrial NADH/NAD⁺ circulator (**Fig. 2l-n and Extended Data Fig. 3j**). The RNA-protein binding assay using cell lysates or recombinant MDH2 verified the direct interaction between *GAS5* and MDH2 both *in vivo* and *in vitro* (**Fig. 2m, n**). The specific interaction between *GAS5* and MDH2 was also controlled by glucose, as indicated by the RNA immunoprecipitation (RIP) assay (**Fig. 2l and Extended Data Fig. 3j**). As shown in **Extended Data Fig. 3k, l**, there were around 1828 copies of *GAS5* per HEK293T cell, which was of relatively high abundance compared with several known functional lncRNAs: *LINK-A* as roughly 150 copy per MDA-MB-231 cell¹⁴ and *CamK-A* as roughly 937 per MDA-MB-231 cell¹⁶. These pieces of evidence suggested that mitochondrial *GAS5* might regulate MDH2-associated metabolism.

The MDH2-binding motif sequence of *GAS5* was identified in the *Loop2* (*GAS5-L2*, 269-465 nt) referred to the *GAS5* secondary structure map (**Fig. 2o and Extended Data Fig. 3m, n**). To identify the region required for *GAS5*'s mitochondrial localization, we generated *GAS5* knock-out (*GAS5-KO*) HEK293T cell lines (**Extended Data Fig. 3o**). Notably, RNA FISH and mitochondria fraction RT-qPCR detection in *GAS5* and its mutants (*GAS5-D1, D2, D3*) rescued *GAS5-KO* HEK293T cells revealed that *Loop2*-deleted *GAS5* (*GAS5-D2*), rather than *Loop1* or *Loop3*-truncated *GAS5*, lost its mitochondrial translocation availability (**Fig. 2p-r and Extended Data Fig. 3p**). It suggested the crucial role of *Loop2* for *GAS5* to function in mitochondria-associated metabolic processes.

GAS5 regulates the FH-MDH2-CS tandem association to modulate mitochondrial metabolism.

Next, we examined the role of MDH2 in mitochondrial TCA cycling. As for the standard Gibbs free energy (ΔG^0) of the TCA cycle steps (**Fig. 3a**), we found that the ΔG^0 of MDH2 node was a highly positive value, suggesting that the forward reaction was theoretically unspontaneous *in vitro*. However, the *in vivo* ΔG of MDH2 node was almost 0, where the rapid oxaloacetate (OAA) consumption by citrate synthase (CS) and sufficient malate supply by fumarate hydratase (FH) might count³¹. As expected, these three canonical members (FH-MDH2-CS) of mitochondrial TCA cycling were colocalized with mitochondria, and they were found to have a considerably high colocalization statistical index (**Extended Data Fig. 4a-i**). We then performed the co-immunoprecipitation (co-IP) assay in the isolated mitochondria fraction and found FH-MDH2-CS robustly associated with each other in mitochondria (**Fig. 3b and Extended Data Fig. 4j**). Their physical interaction was further confirmed by *in vitro* protein pulldown assay (**Fig. 3c, d**). Besides, through mapping the CS interaction associated domain of MDH2 by co-IP assay, the enzyme activity core region (containing substrates binding sites, referring to PDB: 4WLE, 4WLF, 4WLU, 4WLV, 4WLN, and 4WLO MDH2 structure models) along with the MLS (mitochondria location signal peptides, 1-24 amino acid) of MDH2 was available for its interaction with CS (**Extended Data Fig. 4k, l**), suggesting their tight metabolic association. This complex formation was remarkably sensitive to glucose supply conditions (**Extended**

Data Fig. 4m, n), suggesting that this flexible FH-MDH2-CS complex formation facilitated an efficient metabolite stream modulation under various energy situations (**Fig. 3e**).

Interestingly, overexpression of *GAS5-FL* but not its *Loop2*-deletion mutant (*GAS5-D2*) could mimic the energy stress stimulation to block the FH-MDH2-CS complex formation (**Fig. 3f, g and Extended Data Fig. 4p, q**). However, *GAS5* showed a mild effect on MDH2 enzyme activity *in vitro* (**Extended Data Fig. 4o**). Consistently, *GAS5* knockdown significantly attenuated the disintegration of the FH-MDH2-CS complex under glucose starvation (**Fig. 3h, i**) and caused the ectopic malate and citrate level (**Fig. 3j, k**).

Next, we further confirmed the specific metabolic function of mitochondria-distributed *GAS5* in the *GAS5* knockout HEK293T cell. Reconstituting *GAS5* could rescue the FH-MDH2-CS complex formation and the cellular level of ectopic malate/citrate, but this was not the case for the *GAS5-D2* mutant (**Fig. 3l-q and Extended Data Fig. 3p**). The cell growth assay further highlighted that the *Loop2*-dependent mitochondrial distribution of *GAS5* was vital for its mitochondrial metabolic function (**Fig. 3r**). Given the similar phenotype observed between the *GAS5-D2*- and *EV*-transduced cells, the mitochondrial metabolic function of *GAS5* mainly contributed to its inhibitory role in growth control (**Fig. 3r**). Thus, we indicated that mitochondrial *GAS5* could transmit the energy stress signal, disrupt the FH-MDH2-CS complex formation, and eventually inhibit the mitochondria metabolism and cell growth (**Fig. 4s**).

***GAS5* regulates the FH-MDH2-CS complex formation by targeting the MDH2 acetylation.**

We next investigated the molecular mechanism underlying the *GAS5*-impaired FH-MDH2-CS complex formation. Accumulating studies suggested that the metabolic process was associated with the reversible acetylation of metabolic enzymes in cells controlled by cellular energy status³²⁻³⁴. It was known that the acetylation of MDH2 at K185, K301, K307, and K314 were essential for its enzymatic activity³⁴, which was highlighted in red in the 3D molecule model of the acetylated MDH2 (**Extended Data Fig. 5a**). Considering the acetylation of MDH2 was remarkably impaired under glucose starvation and robustly boosted under glucose treatment (**Fig. 4a and Extended Data Fig. 5b**), we hypothesized that MDH2 acetylation could be regulated by mitochondrial *GAS5*. Indeed, loss of *GAS5* dramatically promoted MDH2 acetylation as controlled by glucose (**Fig. 4b and Extended Data Fig. 5c**), while overexpression of *GAS5*, but not *GAS5-D2*, resembled the effect of energy stress in decreasing the MDH2 acetylation (**Extended Data Fig. 4d**). Similarly, re-expressing *GAS5*, but not *GAS5-D2*, rescued the MDH2 acetylation in the *GAS5*-KO HEK293T cell (**Fig. 4c**). Thus, *GAS5* regulated TCA flux metabolic process, probably by negatively regulating MDH2 acetylation in response to energy stress.

Interestingly, we found that the treatment of nicotinamide (NAM, an inhibitor of SIRT6) but not Trichostatin A (TSA, an inhibitor of HDACs) not only artificially increased the acetylation of MDH2 (**Fig. 4d**) but also strikingly strengthen the FH-MDH2-CS complex formation (**Fig. 4e**). To further investigate MDH2 acetylation's effect on the FH-MDH2-CS complex formation, we generated a 4KR mutant to disrupt the MDH2 acetylation sites (K185, K301, K307, and K314) (**Fig. 4f**). In contrast to wild-type MDH2 (MDH2 WT), the 4KR mutant significantly lost the ability to maintain the FH-MDH2-CS complex formation under

NAM treatment (**Fig. 4g, h**). As the acetylation of CS and FH was not sensitive or abundant enough (**Extended Data Fig. 5e, f**), these findings further indicated *GAS5* impaired the FH-MDH2-CS complex formation by declining the acetylation of MDH2.

***GAS5* regulates the FH-MDH2-CS complex formation by increasing the SIRT3-mediated MDH2 deacetylation.**

Because NAM (an inhibitor of SIRT) treatment promoted MDH2 acetylation (**Fig. 4d**), we next examined if the SIRT deacetylase family (*e.g.*, SIRT1-7) regulated MDH2 acetylation. Interestingly, SIRT3 specifically decreased the MDH2 acetylation *in vivo* and *in vitro* (**Fig. 4i-k**). Glucose starvation promoted the SIRT3-MDH2 association (**Fig. 4m, n**). In addition, the SIRT3-MDH2 interaction also affected the CS-MDH2-FH complex formation (**Fig. 4l**). Notably, loss of *GAS5* robustly attenuated the association between SIRT3 and MDH2, especially under glucose starvation condition (**Fig. 4m, n**), while overexpression of *GAS5* enhanced the MDH2-SIRT3 interaction in both wild-type and *GAS5*KO HEK293T cell lines (**Fig. 4o, p**). Moreover, full-length *GAS5* (*GAS5-FL*), but not *GAS5-D2*, promoted SIRT3 recruitment to MDH2 and impaired the FH-MDH2-CS complex formation (**Fig. 4q, r**). These pieces of evidence indicated that *GAS5* could transduce cellular energy status to regulate the SIRT3-MDH2 association, modulate MDH2 deacetylation, and eventually control the FH-MDH2-CS complex formation (**Fig. 4s**).

The role of *GAS5* in modulating mitochondrial metabolism depends on its mitochondria localization.

GAS5 was found to bind the DNA-binding domain of the glucocorticoid receptor (GR) to inhibit the DNA binding of GR through *GAS5-GRE* (included in 546-566 nt) region²². Notably, the indicated GR-associated region of *GAS5* (*GAS5-GRE*) was comprised in the *GAS5-Loop3* (546-634 nt); however, the *GAS5-D3* ($\Delta L3$, $\Delta 546-634$ nt) mutant showed a limited effect on MDH2-SIRT3 interaction (**Fig. 4p**), MDH2 acetylation (**Fig. 4c**), FH-MDH2-CS association (**Fig. 3l, m**) and mitochondrial metabolites streaming (**Fig. 3n-q**). Furthermore, we showed that the cell growth effect of the *GAS5-D3* mutant was similar to that of the full-length *GAS5* (*GAS5-FL*) (**Fig. 3r**). Given the *GAS5-Loop2* region's essential role in regulating *GAS5*'s mitochondrial localization and its associated downstream signaling events (**Fig. 3l, m, 4c, p, 3n-r**), our findings suggested that the function of mitochondrial *GAS5* was independent on GR.

Mitochondria-associated *GAS5* inhibits breast tumorigenesis by restricting TCA flux.

Mitochondria metabolism was critical for tumor progression³⁵, and *GAS5* was associated with human cancer progression, including breast cancer³⁶. Besides, *GAS5* was found with around 1099 copy per MDA-MB-231 cell and 1272 per MDA-MB-468 cell (**Extended Data Fig. 3k, l**), which were relatively high abundances as compared with other known cancer-related lncRNAs such as *LINK-A* (roughly 150 copy per MDA-MB-231 cell) and *CamK-A* (roughly 937 per MDA-MB-231 cell)^{14,16}. Therefore, we examined the role of *GAS5* in breast cancer development. Consistently, tumorous *GAS5* was glucose-sensitive and able to enter mitochondria to suppress the CS-MDH2-FH complex formation (**Fig. 5a-e and Extended Data Fig. 6a**). Overexpressing *GAS5* resulted in increased malate and decreased citrate in human breast cancer cell line MDA-MB-231 (**Fig. 5f, g**). Overexpression of *GAS5* in MDA-MB-231 cells suppressed the generation of

NADH and subsequently decreased mitochondrial ATP production (**Fig. 5h, i and Extended Data Fig. 5b-e**). Similar findings were observed in the mitochondria respiration assay (**Extended Data Fig. 6f**) and another human breast cancer cell line MDA-MB-468 (**Extended Data Fig. 6g-m**). Furthermore, overexpression of *GAS5* inhibited tumor proliferation and anchorage-independent growth of breast cancer cells (**Extended Data Fig. 6n, o**). Collectively, these results indicated that *GAS5* functioned as a key regulator of breast cancer metabolism to control breast tumorigenesis.

Given mitochondrial MDH2 was the critical effector of *GAS5* (**Fig. 2-4**), we examined whether MDH2 was required for the *GAS5*-mediated breast cancer suppression. The citrate/malate detection assay and the colony formation assay showed that expressing MDH2, but not its 4KR mutant, significantly attenuated the inhibitory role of *GAS5* in regulating malate/citrate level and tumor cell growth (**Fig. 5j-l**). Furthermore, although *GAS5* could partly mimic the metabolic impact caused by energy stress, citrate restoration could significantly rescue the cell growth in the context of *GAS5* overexpression (**Extended Data Fig. 6p**), suggesting that the citric acid cycle functions downstream of *GAS5*. Consistent with tumor cell growth assay (**Fig. 5l and Extended Data Fig. 6n, o**), overexpression of *GAS5* suppressed both the size and weight of the xenograft tumors (**Fig. 5m, n and Extended Data Fig. 6q**), and significantly reduced cell proliferation as indicated by IHC proliferation indexes (i.e., Ki67 and Cyclin D1) (**Fig. 5o, p**) and RT-qPCR analysis (**Extended Data Fig. 6r**). In addition, the angiogenesis marker CD31 level was also down-regulated upon overexpression of *GAS5* (**Fig. 5o, p**). Also, MDH2, but not its 4KR mutant, significantly attenuated the tumor suppressor role of *GAS5 in vivo* (**Fig. 5m-p and Extended Data Fig. 6q, r**). Collectively, these results demonstrated a tumor suppressor role of mitochondrial *GAS5* by modulating mitochondria TCA cycling.

High expression of *GAS5* and low TCA flux benefit clinical outcomes in breast cancer patients

Next, we examined *GAS5* and TCA metabolism enzymes' expression levels in a cohort of breast cancer tissues obtained from Sun Yat-sen University Cancer Center (SYSUCC) (**Supplementary Table 3**). Downregulation of *GAS5* was found in breast cancer tumors compared with the corresponding adjacent normal tissues (**Fig. 6a**; n = 48). We divided the patients into two groups (*GAS5*-low and *GAS5*-high), based on the expression of *GAS5* compared to the median value of all patients. The *GAS5*-high group showed a better survival rate than the *GAS5*-low group (**Fig. 6b**; n = 200). The immunohistochemistry (IHC) analysis further confirmed that tumors with low *GAS5* expression harbored a high level of MDH2 and progression markers (i.e., Ki67 and Cyclin D1) (**Fig. 6c, d**; n = 200). Therefore, these results showed an inverse relationship between *GAS5* and tumor progress.

We also examined the MDH2 expression in breast tumors and normal tissues by RT-qPCR (**Fig. 6e**; n = 48) and IHC (**Extended Data Fig. 6w**; n = 100) in a cohort of breast cancer tissues, finding that MDH2 was upregulated in the advanced breast tissues. Moreover, we categorized the patients into two groups (MDH2-low and MDH2-high) based on the expression of MDH2 and found that low MDH2 level benefited the overall survival rate of breast cancer patients (**Fig. 6f**; n = 200). The IHC staining assay also revealed the high MDH2 expression in a subset (MDH2-high subset) of breast cancer tissues (**New Fig. 6g**; n =

200). Moreover, tumors with high MDH2 expression also showed a high expression of cell proliferation markers (i.e., Ki67 and Cyclin D1) (**Fig. 6g, h**). Notably, FH and CS were also found highly expressed in the advanced breast cancer tissues (**Fig. 6i, j, and Extended Data Fig. 6v, w**), while SIRT3 was found down-regulated there (**Extended Data Fig. 6s, t**). These results suggested that high levels of MDH2, CS, and FH favored tumor progress, and SIRT3 negatively regulated the FH-MDH2-CS complex in both cells and tumors.

A further subgroup of breast cancer patients was conducted to investigate the relationship between *GAS5*-MDH2 and the patient survival rate. Notably, patients with the low level of MDH2 and high level of *GAS5* were significantly associated with a better survival rate (**Fig. 6k**; $n = 200$, $P < 0.001$) as compared with that of individual *GAS5* (**Fig. 6b**, $n = 200$, $P = 0.0039$) or MDH2 (**Fig. 6f**, $n = 200$, $P = 0.0198$). Collectively, these data suggested that the mitochondria-associated *GAS5*-MDH2 axis was involved in breast cancer metabolism and tumorigenesis (**Fig. 6l**), highlighting its potential diagnostic marker and therapeutic target roles for breast cancer.

Discussion

Membrane-enclosed organelles, such as the mitochondria, endoplasmic reticulum (ER), lysosome, and Golgi, define various critical cellular processes⁷. Comprehensively exploring the components of organelles will unveil substantial clues underlying cellular function and human diseases. Traditional approaches, despite the developed density medium from sucrose to Percoll, often result in contamination across fractionations^{37,38}. However, the approximation of the sedimentation coefficient between organelles (e.g., mitochondria and lysosome), especially the membrane-less granules, frequently compromises the sensitivity in the RNA detection. The previous study of mitochondria RNAs treated the density-centrifuged pellet with RNase to clear the outer RNAs²¹. However, the membrane-anchored RNAs were ablated, and the membrane-less granules with resistance to RNase would remain. In this study, we developed an effective organelle isolation method to obtain the non-artificial treatment subcellular components by combining centrifugation with endogenous immunoprecipitation using specific organelle protein markers. Recent developments applied proximity labeling techniques coupled proteomics to a subcellular RNAs study^{27,39}. However, it required exogenous transduction and chemical treatment. Compared with them^{27,40}, our method does not rely on additional biochemistry treatment or cell transfection; therefore, it is more suitable and convenient for investigating the bona fide cellular events under physiological conditions, including energy sources, drugs, and cytokines.

Using this approach, we identified thousands of organelle-associated RNAs, especially the subcellular lncRNAs that might function in numerous essential cellular processes. Notably, most of these newly identified lncRNAs were missed in the studies using either the APEX-RIP-Seq or the newly APEX-Seq^{27,39}. As the emerging pivotal roles of lysosome and mitochondria in regulating cellular energy homeostasis^{2,10,29,41}, the identified mitochondria- and lysosome-associated lncRNA sets could function as messengers and regulators in organelle communication and cellular metabolism processes.

Among them, we identified a mitochondria-associated lncRNA named *GAS5*. *GAS5* was identified in a subtraction cDNA library that hosts differentially expressed genes in growth-arrested cells⁴² and was then characterized as a universal tumor suppressor⁴³. Mechanistically, *GAS5* was found to act as a DNA decoy for glucocorticoid receptor (GR) in response to growth factors²², regulate insulin receptor (*INSR*) gene transcription in adipocytes²³, and act as an RNA sponger to buffer miRNAs²⁴. However, these limited results were still hard to explain its roles in the unique cellular localization and glucose metabolism. Excitingly, we found mitochondria-associated lncRNA *GAS5* could respond to the glucose condition and regulate TCA flux by suppressing the FH-MDH2-CS complex formation, which largely contributed to its tumor suppressor function (**Fig. 3r, s**).

Glycolysis, with actually low absolute energy generation efficiency, provides abundant intermediate metabolites and NADPH for anabolism and it is usually highly activated in cancers³⁵. However, previous studies had found that members of the mitochondrial TCA cycle could benefit tumors in non-canonical ways^{44,45}. It was also shown that *GAS5* overexpression took no significant effect on glycolysis⁴⁶. Strikingly, our findings showed that mitochondrial TCA cycle enzymes FH/CS/MDH2 were all upregulated in tumor tissues (**Fig. 6e, i, j, and Extended Data Fig. 6u-w**) and *GAS5* could suppress cell growth by directly blocking the TCA cycle by controlling these enzymes. Besides, mitochondria metabolism-regulated ATP, NAD(P)⁺/NAD(P)H, and intermediate metabolites were also critical for macromolecular synthesis and redox control during cell growth and proliferation. Together with the previous studies^{41,44,45,47,48}, our findings proposed that the mitochondrial TCA cycle was both sufficient and necessary for tumor development in both canonical metabolism manner and non-canonical manner. Given the crucial role of this uncovered mitochondria-associated lncRNA in regulating breast cancer mechanism and progression, our study paradigm-shifts our current understanding of the mitochondrial TCA cycle in physiology and cancer.

Declarations

ACKNOWLEDGMENTS

We would like to thank Tian-hua Zhou (Zhejiang University), Jun Huang (Zhejiang University) and Ping-long Xu (Zhejiang University) for their support and suggestion on this study. We thank Prof. Jia-huai Han (Xiamen University) for gifting CS and FH template vectors. We thank Prof. Xu Li (Westlake University) for gifting SIRT6 vectors and assistance for protein MS analysis. We thank Hai-long Piao (Chinese Academy of Science) for metabolites analysis. We also thank Cipher Gene, LLC, for the support in generating and processing the RNA-seq data, and for the help in data interpretation. This work was supported in part by the National Natural Science Foundation of China (81672791, 81872300), Zhejiang Provincial Natural Science Fund for Distinguished Young Scholars of China (LR18C060002) to A.L. A.L. is a scholar of Thousand Youth Talents-China, a scholar of Thousand Talents-Zhejiang, a scholar of Hundred Talents-Zhejiang University.

AUTHOR CONTRIBUTIONS

A.L. conceived and designed the research. L.-J.S., H.-Q.J., and Z.-Z.Y. performed most of the biochemical, molecular experiments and bioinformatics analysis, with the assistance from Q.-W.G., Z.Z., F.-Z.L., L.-J.Y., H.-D.G., C.-Y.S., L.Q., L.-J.Y., H.C., H.C., M.-J.W., R.-H.L. and Q.-Q.Z.. H.-Q.J. performed clinical specimens ascertain and process. Z.-Z.Y., L.Q. and W.-S.Y. conducted the bioinformatics analysis. L.-J.S. and F.-Z.L. performed xenograft experiments and immunohistochemistry analyses. T.Z., W.W., J.L., J.-Z.S., Q.-F.Y., H.-Q.J., and H.-L.P contributed to discussion and data interpretation. T.Z., W.W., and J.L. edited the manuscript. A.L. wrote the manuscript.

DECLARATION OF INTERESTS

The authors declare no competing interests.

References

- 1 Birsoy, K. *et al.* An Essential Role of the Mitochondrial Electron Transport Chain in Cell Proliferation Is to Enable Aspartate Synthesis. *Cell* **162**, 540-551, doi:10.1016/j.cell.2015.07.016 (2015).
- 2 Ballabio, A. & Bonifacino, J. S. Lysosomes as dynamic regulators of cell and organismal homeostasis. *Nature Reviews Molecular Cell Biology*, doi:10.1038/s41580-019-0185-4 (2019).
- 3 Perera, R. M. & Zoncu, R. The Lysosome as a Regulatory Hub. *Annu Rev Cell Dev Bi* **32**, 223-253, doi:10.1146/annurev-cellbio-111315-125125 (2016).
- 4 Boyman, L., Karbowski, M. & Lederer, W. J. Regulation of Mitochondrial ATP Production: Ca(2+) Signaling and Quality Control. *Trends Mol Med*, doi:10.1016/j.molmed.2019.10.007 (2019).
- 5 Stevenson, J., Huang, E. Y. & Olzmann, J. A. Endoplasmic Reticulum-Associated Degradation and Lipid Homeostasis. *Annu Rev Nutr* **36**, 511-542, doi:10.1146/annurev-nutr-071715-051030 (2016).
- 6 Zong, Y. *et al.* Hierarchical activation of compartmentalized pools of AMPK depends on severity of nutrient or energy stress. *Cell Res* **29**, 460-473, doi:10.1038/s41422-019-0163-6 (2019).
- 7 Mottis, A., Herzig, S. & Auwerx, J. Mitocellular communication: Shaping health and disease. *Science* **366**, 827-832, doi:10.1126/science.aax3768 (2019).
- 8 Efeyan, A., Zoncu, R. & Sabatini, D. M. Amino acids and mTORC1: from lysosomes to disease. *Trends Mol Med* **18**, 524-533, doi:10.1016/j.molmed.2012.05.007 (2012).
- 9 Thul, P. J. *et al.* A subcellular map of the human proteome. *Science* **356**, doi:10.1126/science.aal3321 (2017).
- 10 Zhang, C. S. *et al.* Fructose-1,6-bisphosphate and aldolase mediate glucose sensing by AMPK. *Nature* **548**, 112+, doi:10.1038/nature23275 (2017).

- 11 Wyant, G. A. *et al.* mTORC1 Activator SLC38A9 Is Required to Efflux Essential Amino Acids from Lysosomes and Use Protein as a Nutrient. *Cell* **171**, 642-654 e612, doi:10.1016/j.cell.2017.09.046 (2017).
- 12 Wang, S. *et al.* Metabolism. Lysosomal amino acid transporter SLC38A9 signals arginine sufficiency to mTORC1. *Science* **347**, 188-194, doi:10.1126/science.1257132 (2015).
- 13 Wagner, G. R. *et al.* A Class of Reactive Acyl-CoA Species Reveals the Non-enzymatic Origins of Protein Acylation. *Cell Metab* **25**, 823-837 e828, doi:10.1016/j.cmet.2017.03.006 (2017).
- 14 Lin, A. *et al.* The LINK-A lncRNA interacts with PtdIns(3,4,5)P3 to hyperactivate AKT and confer resistance to AKT inhibitors. *Nat Cell Biol* **19**, 238-251, doi:10.1038/ncb3473 (2017).
- 15 Lin, A. *et al.* The LINK-A lncRNA activates normoxic HIF1 α signalling in triple-negative breast cancer. *Nat Cell Biol* **18**, 213-224, doi:10.1038/ncb3295 (2016).
- 16 Sang, L. J. *et al.* lncRNA CamK-A Regulates Ca²⁺-Signaling-Mediated Tumor Microenvironment Remodeling. *Mol Cell* **72**, 71-83 e77, doi:10.1016/j.molcel.2018.08.014 (2018).
- 17 Ma, Y., Zhang, J., Wen, L. & Lin, A. Membrane-lipid associated lncRNA: A new regulator in cancer signaling. *Cancer Lett* **419**, 27-29, doi:10.1016/j.canlet.2018.01.008 (2018).
- 18 Chen, X. *et al.* Visualizing RNA dynamics in live cells with bright and stable fluorescent RNAs. *Nat Biotechnol* **37**, 1287-1293, doi:10.1038/s41587-019-0249-1 (2019).
- 19 Hocine, S., Raymond, P., Zenklusen, D., Chao, J. A. & Singer, R. H. Single-molecule analysis of gene expression using two-color RNA labeling in live yeast. *Nature Methods* **10**, 119-121, doi:DOI 10.1038/nmeth.2305 (2013).
- 20 Chen, K. H., Boettiger, A. N., Moffitt, J. R., Wang, S. & Zhuang, X. RNA imaging. Spatially resolved, highly multiplexed RNA profiling in single cells. *Science* **348**, aaa6090, doi:10.1126/science.aaa6090 (2015).
- 21 Mercer, T. R. *et al.* The human mitochondrial transcriptome. *Cell* **146**, 645-658, doi:10.1016/j.cell.2011.06.051 (2011).
- 22 Kino, T., Hurt, D. E., Ichijo, T., Nader, N. & Chrousos, G. P. Noncoding RNA gas5 is a growth arrest- and starvation-associated repressor of the glucocorticoid receptor. *Sci Signal* **3**, ra8, doi:10.1126/scisignal.2000568 (2010).
- 23 Patel, N., Murr, M., Lui, A., Shi, Y. & Cai, J. OR01-6 lncRNA GAS5 Directed Therapeutic Increases Insulin Receptor Expression in Adipocytes. *Journal of the Endocrine Society* **3**, doi:10.1210/js.2019-OR01-6 (2019).

- 24 Zhao, H. *et al.* Lowly-expressed lncRNA GAS5 facilitates progression of ovarian cancer through targeting miR-196-5p and thereby regulating HOXA5. *Gynecol Oncol* **151**, 345-355, doi:10.1016/j.ygyno.2018.08.032 (2018).
- 25 Yoshida, H. ER stress and diseases. *FEBS J* **274**, 630-658, doi:10.1111/j.1742-4658.2007.05639.x (2007).
- 26 Bethune, J., Jansen, R. P., Feldbrugge, M. & Zarnack, K. Membrane-Associated RNA-Binding Proteins Orchestrate Organelle-Coupled Translation. *Trends Cell Biol* **29**, 178-188, doi:10.1016/j.tcb.2018.10.005 (2019).
- 27 Fazal, F. M. *et al.* Atlas of Subcellular RNA Localization Revealed by APEX-Seq. *Cell* **178**, 473-490 e426, doi:10.1016/j.cell.2019.05.027 (2019).
- 28 Love, M. I., Huber, W. & Anders, S. Moderated estimation of fold change and dispersion for RNA-seq data with DESeq2. *Genome Biol* **15**, 550, doi:10.1186/s13059-014-0550-8 (2014).
- 29 Weinberg, S. E. & Chandel, N. S. Targeting mitochondria metabolism for cancer therapy. *Nat Chem Biol* **11**, 9-15, doi:10.1038/nchembio.1712 (2015).
- 30 Xing, Z. *et al.* lncRNA directs cooperative epigenetic regulation downstream of chemokine signals. *Cell* **159**, 1110-1125, doi:10.1016/j.cell.2014.10.013 (2014).
- 31 Nelson, D. L., Cox, M. M. & Lehninger, A. L. *Lehninger principles of biochemistry*. Seventh edition. edn, (W.H. Freeman and Company ; Macmillan Higher Education, 2017).
- 32 Lv, L. *et al.* Acetylation targets the M2 isoform of pyruvate kinase for degradation through chaperone-mediated autophagy and promotes tumor growth. *Mol Cell* **42**, 719-730, doi:10.1016/j.molcel.2011.04.025 (2011).
- 33 Someya, S. *et al.* Sirt3 mediates reduction of oxidative damage and prevention of age-related hearing loss under caloric restriction. *Cell* **143**, 802-812, doi:10.1016/j.cell.2010.10.002 (2010).
- 34 Zhao, S. *et al.* Regulation of cellular metabolism by protein lysine acetylation. *Science* **327**, 1000-1004, doi:10.1126/science.1179689 (2010).
- 35 Vander Heiden, M. G., Cantley, L. C. & Thompson, C. B. Understanding the Warburg effect: the metabolic requirements of cell proliferation. *Science* **324**, 1029-1033, doi:10.1126/science.1160809 (2009).
- 36 Mourtada-Maarabouni, M., Pickard, M. R., Hedge, V. L., Farzaneh, F. & Williams, G. T. GAS5, a non-protein-coding RNA, controls apoptosis and is downregulated in breast cancer. *Oncogene* **28**, 195-208,

doi:10.1038/onc.2008.373 (2009).

37 Graham, J. M. *Biological centrifugation*. (Bios, 2001).

38 Work, T. S. & Work, E. *Laboratory techniques in biochemistry and molecular biology*. (North-Holland Pub. Co., 1969).

39 Kaewsapsak, P., Shechner, D. M., Mallard, W., Rinn, J. L. & Ting, A. Y. Live-cell mapping of organelle-associated RNAs via proximity biotinylation combined with protein-RNA crosslinking. *Elife* **6**, doi:10.7554/eLife.29224 (2017).

40 Chen, W. W., Freinkman, E., Wang, T., Birsoy, K. & Sabatini, D. M. Absolute Quantification of Matrix Metabolites Reveals the Dynamics of Mitochondrial Metabolism. *Cell* **166**, 1324-1337 e1311, doi:10.1016/j.cell.2016.07.040 (2016).

41 Ryan, D. G. *et al.* Coupling Krebs cycle metabolites to signalling in immunity and cancer. *Nat Metab* **1**, 16-33, doi:10.1038/s42255-018-0014-7 (2019).

42 Schneider, C., King, R. M. & Philipson, L. Genes Specifically Expressed at Growth Arrest of Mammalian-Cells. *Cell* **54**, 787-793, doi:10.1016/S0092-8674(88)91065-3 (1988).

43 Yu, X. & Li, Z. Long non-coding RNA growth arrest-specific transcript 5 in tumor biology (Review). *Oncol Lett* **10**, 1953-1958, doi:10.3892/ol.2015.3553 (2015).

44 Wang, T. *et al.* O-GlcNAcylation of fumarase maintains tumour growth under glucose deficiency. *Nat Cell Biol* **19**, 833-843, doi:10.1038/ncb3562 (2017).

45 Wang, Y. *et al.* KAT2A coupled with the alpha-KGDH complex acts as a histone H3 succinyltransferase. *Nature* **552**, 273-277, doi:10.1038/nature25003 (2017).

46 Zhang, X. C. *et al.* YY1/LncRNA GAS5 complex aggravates cerebral ischemia/reperfusion injury through enhancing neuronal glycolysis. *Neuropharmacology* **158**, 107682, doi:10.1016/j.neuropharm.2019.107682 (2019).

47 Xiao, Z., Dai, Z. & Locasale, J. W. Metabolic landscape of the tumor microenvironment at single cell resolution. *Nat Commun* **10**, 3763, doi:10.1038/s41467-019-11738-0 (2019).

48 Etchegaray, J. P. & Mostoslavsky, R. Interplay between Metabolism and Epigenetics: A Nuclear Adaptation to Environmental Changes. *Mol Cell* **62**, 695-711, doi:10.1016/j.molcel.2016.05.029 (2016).

49 Pertea, M., Kim, D., Pertea, G. M., Leek, J. T. & Salzberg, S. L. Transcript-level expression analysis of RNA-seq experiments with HISAT, StringTie and Ballgown. *Nat Protoc* **11**, 1650-1667, doi:10.1038/nprot.2016.095 (2016).

- 50 Sun, L. *et al.* Utilizing sequence intrinsic composition to classify protein-coding and long non-coding transcripts. *Nucleic Acids Res* **41**, e166, doi:10.1093/nar/gkt646 (2013).
- 51 Kong, L. *et al.* CPC: assess the protein-coding potential of transcripts using sequence features and support vector machine. *Nucleic Acids Res* **35**, W345-349, doi:10.1093/nar/gkm391 (2007).
- 52 The Gene Ontology, C. The Gene Ontology Resource: 20 years and still GOing strong. *Nucleic Acids Res* **47**, D330-D338, doi:10.1093/nar/gky1055 (2019).
- 53 Kanehisa, M. *et al.* From genomics to chemical genomics: new developments in KEGG. *Nucleic Acids Res* **34**, D354-357, doi:10.1093/nar/gkj102 (2006).
- 54 Li, C. *et al.* A ROR1-HER3-lncRNA signalling axis modulates the Hippo-YAP pathway to regulate bone metastasis. *Nat Cell Biol* **19**, 106-119, doi:10.1038/ncb3464 (2017).

Methods

CONTACT FOR REAGENT AND RESOURCE SHARING

Further information and requests for resources and reagents should be directed to and will be fulfilled by the Lead Contact, Aifu Lin (linaifu@zju.edu.cn).

EXPERIMENTAL MODEL AND SUBJECT DETAILS

Cell lines

Human breast cancer cell lines MDA-MB-231 (Cat#CRM-HTB-26; RRID: CVCL_0062), MDA-MB-468 (Cat#HTB-132; RRID: CVCL_0419), and human embryonic kidney cell line HEK293T (Cat#CRL-3216; RRID: CVCL_0063) were purchased from American Type Culture Collection (ATCC) and characterized by Cell Line Core Facility (MD Anderson Cancer Center). These cell lines were maintained in Dulbecco modified essential medium (DMEM) supplemented with 10% fetal bovine serum (FBS) at 37 °C in 5% CO₂ (v/v). All cells were negatively tested for mycoplasma contamination and authenticated based on STR fingerprinting before use.

Tissue Samples

Fresh frozen breast cancer tissues (Sun Yat-sen Cohorts) were obtained from Sun Yat-sen University Cancer Center (SYSUCC) as previously described¹⁶. The study protocol was approved by the Institutional Review Board of Sun Yat-sen University Cancer Center. All tissue samples were collected in compliance with informed consent policy. Detailed clinical information is listed in **Supplementary Table 3**.

Mice

All animal experiments were performed in accordance with a protocol approved by the Institutional Animal Care. Care of experimental animals was in accordance with guidelines and approved by the Laboratory Animal Committee of Zhejiang University. Female nude mice (4-5 weeks old) were purchased from the Shanghai SLAC Laboratory Animal Co., Ltd.

METHOD DETAILS

Antibodies

Specific antibodies were purchased from the following commercial sources for indicating experiments: anti-MDH2 (ab110317, 1:100 for IP), anti-MDH2 (ab181857, 1:2000 for IB, 1:100 for IHC), anti-CS (ab129095, 1:2000 for IB, 1:100 for IHC), anti-FH (ab233394, 1: 2000 for IB, 1:100 for IHC), Goat anti-Rabbit IgG H&L (Alexa Fluor[®] 488) (150077, 1:400 for IF), Goat anti-Rabbit IgG H&L (Alexa Fluor[®] 594) (150080, 1:400 for IF), Goat anti-Mouse IgG H&L (Alexa Fluor[®] 488) (150113, 1:400 for IF), Goat anti-Mouse IgG H&L (Alexa Fluor[®] 594) (150116, 1:400 for IF) from Abcam; anti-Acetylated-Lysine (9441, 1:1000 for IB), anti-LAMP1 (9091, 1:2000 for IB, 1:50 for IP, 1:50 for IF), anti-Tom20 (42406, 1:2000 for IB, 1:50 for IP, 1:50 for IF), anti-Vinculin (13901, 1:2000 for IB), anti-Lamin B1 (12586, 1:2000 for IB), anti-Cyclin D1 (55506, 1:100 for IHC), anti-Ki67 (9449, 1:100 for IHC), anti-CD31 (77699S, 1:100 for IHC), anti-Calnexin (2679, 1:2000 for IB) from Cell Signaling Technology; anti-His-tag (M20001, 1:5000 for IB), anti-Myc-tag (M20002, 1:5000 for IB), anti-DYKDDDDK-tag (M20008, 1:10000 for IB), anti-HA-tag (M20003, 1:5000 for IB), anti-GFP-tag (M20004, 1:5000 for IB), anti-GAPDH (M20050, 1:5000 for IB) from abmart; anti-LAMP2 (sc-18822, 1:200 for IB, 1:20 for IF) from Santa Cruz Biotechnology; Streptavidin-HRP (21130, 1:5000 for IB) from Thermo Fisher Scientific; HRP Goat anti-Mouse IgG (H+L) (BK-R050, 1:5000 for IB), HRP Goat anti-Rabbit IgG (H+L) (BK-M050, 1:5000 for IB) from Bioker.

Cloning Procedures

The full-length *MDH2* and *GAS5* were cloned from HEK293T cDNA by PCR. *CS*, *FH* full-length template was gifted from Jia-huai Han lab. *SIRT1-7* vectors were gifted from Xu Li lab. All these eukaryotic overexpression genes (wild type and mutants) were cloned into SFB-Iv (S-tag, FLAG-tag and SBP-tag fused) vector using the Gateway system (Invitrogen) and pcDNA3.1-Flag/Myc/HA/His empty vectors using T4 ligase (Promega) or ClonExpress II One Step Cloning Kit (Vazyme). *GAS5* and its deletion mutants were cloned into pGEM-T easy (Promega) for *in vitro* transcription. All single-point and deletion mutations were generated by PCR overlapping. Bacterial expression vectors for MBP-His-tagged MDH2 and SIRT3 (wild type and mutants) were constructed by cloning into pMBP28a vector.

Protein Recombination and Purification

Recombinant proteins His-MBP-MDH2 and SIRT3 (wild type and mutants) were expressed in *E. coli* strain BL21-CodonPlus[®] (DE3)-RIPL (Agilent Technologies) and purified using Ni-NTA Sefnrose Resin (Sangon Biotech), respectively. Human bioactive SFB or FLAG tagged MDH2, CS and FH were purified from overexpression vectors transduced HEK293T cells. Purification was conducted by using FLAG (M2)

magnetic beads (Sigma) to enrich and using 3×FLAG peptide (Sigma) to elute. All the concentration and purity of recombinant proteins were measured by SDS-PAGE and Coomassie staining with the standard BSA control.

LMF, Mitochondria and Lysosome Purification

Cells (at least 10^7) were washed once by KPBS (136 mM KCl, 10 mM KH_2PO_4 , pH 7.25) and harvested by gentle scraping. Cells were pelleted down by centrifugation at 4 °C at 1000 g for 1 min. The cell pellet was resuspended with 500 μl KPBS containing the inhibitor cocktail and subjected to 2 ml Dounce homogenization. 40-50 strokes were sufficient and the efficiency could be monitored by bright field microscopy with trypan blue staining. After homogenization, the cell extraction was transferred to new 1.5 ml EP tubes and centrifuged at 4 °C at 1,000 g for 10 min. The resulting supernatant was reserved and further centrifuged at 4 °C at 1,000 g for 10 min. The resulting supernatant was the indicated LMF suspension. The real LMF pellet (regarded mainly as mitochondria and lysosome mixture) could be obtain by centrifugation at 4 °C at 13,000 g for 5 min.

500 μl above indicated LMF suspension should be incubated with 2 μl Tom20 antibody at 4 °C for 2 hr with gentle rotation, following by adding 20 μl KPBS-precleared protein A/G magnetic beads for further incubation at 4 °C for additional 1 hr rotation. After the incubation, the mitochondria were supposed to be captured and immobilized by Tom20 antibody coated beads. The enriched mitochondria were collected in the pellet of beads while the supernatant were discarded by physically magnetic enrichment. The beads enriched mitochondria should be further washed by pipetting 10 times in 500 μl KPBS. The washing step could be optionally replicated by 3 times and the resulting beads complex was the purified mitochondria fraction.

As the indicated Tom20 antibody was shift into the LAMP1 one, the procedure of the lysosome fraction was largely similar to the mitochondria fraction. However, considering the limiting content of the lysosome in cells, more cells would be additionally in need for better protein and RNA detection.

ER Purification

Over 10^7 cells were harvested and collected in PBS. Pellet down cells and discard the PBS. Resuspend the cells with 3 times volume of cold hypotonic extraction buffer (10 mM HEPES pH 7.8, with 1 mM EGTA and 25 mM potassium chloride) and incubate for 20 min at 4 °C to facilitate the cell swelling. Then, centrifuge at 600 g for 5 min to collect the swelled cells and discard the supernatant. Add a volume of isotonic extraction buffer (10 mM HEPES pH 7.8, 250 mM sucrose, 25 mM potassium chloride, and 1 mM EGTA) to the cells and homogenize the cells with 10-20 strokes in Dounce homogenizer. Centrifuge the homogenate at 1,000 g for 10 min at 4 °C and collect the supernatant in a new tube. Further centrifuge the supernatant at 12,000 g for 15 min at 4 °C and collect the supernatant. This supernatant is almost free of LMF components and was the source for microsomes (the form of ER in *in vitro* isolation processes). Estimate the volume of the indicated supernatant and add 7.5 times volume 8 mM CaCl_2 buffer. Rotate the mixture solution for 20-30 min at 4 °C and flocculent precipitate would gradually appear

which was the ER microsome fraction. Centrifuge at 8,000 g for 10 min at 4 °C and the pellet was the ER microsomes. Remove the supernatant and wash the pellet twice with isotonic extraction buffer to clear the cytosol contaminant. The isolated ER could be used for RNA analysis and Western blot detection.

RNA Isolation and Sequencing

RNA degradation and contamination were monitored on 1% agarose gels; concentration was measured using Qubit[®] RNA Assay Kit in Qubit[®] 2.0 Fluorometer (Life Technologies, CA, USA); RNA integrity was assessed using the RNA Nano 6000 Assay Kit of the Bioanalyzer 2100 system (Agilent Technologies, CA, USA).

A total amount of 1 µg RNA per sample was used as input material for the RNA sample preparations by rRNA depleting method. Libraries were sequenced on an Illumina NovaSeq platform and 150 bp paired-end reads were generated.

Data Analysis

Reference genome and gene model annotation files were downloaded from genome website (<http://hgdownload.soe.ucsc.edu/goldenPath/hg19/bigZips/>) directly. Index of the reference genome was built using HISAT2 (hierarchical indexing for spliced alignment of transcripts) v2.0.4⁴⁹ and paired-end clean reads were aligned to the reference genome using HISAT2 v2.0.4⁴⁹. The mapped reads of each sample were assembled by String Tie v1.2.1⁴⁹, combined all assembled information by String Tie merge v1.2.1, and annotated by gffcompare v0.9.7 using a reference-based approach.

Transcripts predicted to have coding potential by all of the two prediction tools (CNCI (Coding-Non-Coding-Index) (v2)⁵⁰/CPC (Coding Potential Calculator) (0.9-r2)⁵¹) were filtered out, and transcripts with no coding potential were selected as the novel candidate set of lncRNAs.

Ballgown was used to calculate FPKMs of lncRNAs in each sample. Technical replicates were evaluated by scatter plot with FPKM data. Differential genes were analyzed by DESeq2²⁸, fold-change over 1.5 was selected as threshold as differentially expressed. By this criterion, heatmap of expression pattern was generated with R package (pheatmap); overlapping and specific lncRNAs between organelles was shown by Venn and Circos maps.

In order to evaluate our isolation efficiency, LMF was utilized as the traditional fractionation separating method, all 13 mitochondrial genes and 9 Lysosome genes (C12orf66/LAMP2/LAMP3/RAB7A/RHEBL1/RPS6KC1/SNX6/STX7/VPS26A) were selected as marker to assess gene enrichment in our method.

With Gene Ontology and KEGG annotation results, we classify DGEs according to official classification, and we also perform GO⁵² and KEGG⁵³ functional enrichment using clusterProfiler (a package of R program) for both lncRNAs and mRNAs' function.

siRNA, shRNA and RNAi

All siRNAs sequences were designed according to <http://sirna.wi.mit.edu/home.php> and all shRNAs sequences were designed according to <https://portals.broadinstitute.org/gpp/public/>. siRNAs were commercially generated (GenePharma). All shRNAs sequences were cloned into pLKO.1-Puro vector, two shRNA producing the best knockdown efficiency were used in the following functional studies. Detailed sequences were listed in the **Supplementary Table 4**.

Cell Transfection, Treatment and Lentiviral-Based Gene Transduction

Human breast cancer cell lines MDA-MB-231, MDA-MB-468, and human embryonic kidney cell line HEK293T were maintained in Dulbecco modified essential medium (DMEM) supplemented with 10% fetal bovine serum (FBS) at 37 °C in 5% CO₂ (v/v). All cells were negatively tested for mycoplasma contamination and authenticated based on STR fingerprinting before use.

siRNA and plasmid transfections were performed using Lipofectamine[®] 2000 (Life Technologies). Lentiviruses were produced in HEK293T cells with package vectors VSVG and psPAX2. The virus was harvested 48 hr and 72 hr after transfection to transduce HEK293T, MDA-MB-231 or MDA-MB-468 cells, followed by selection with 1 µg/ml puromycin. The stable cell lines with *GAS5* knockdown were verified by RT-qPCR and used for following functional studies.

Cell Lysis, Immunoprecipitation and Immunoblotting

Cells were harvest in PBS and homogenized in NETN buffer (25mM Tris-HCl pH 8.0, 100 mM NaCl, 1 mM EDTA, 0.5 mM DTT) with Protease Inhibitor Cocktail, Phosphatase Inhibitor Cocktail, Panobinostat, and Methylstat. Lysates were cleared by centrifugation at 13,000 g for 15 min at 4 °C. Supernatants could be applied for immunoblotting (IB) or immunoprecipitation (IP) with the indicated antibodies. As for IP, add the required primary antibody and the control IgG separately to the prepared lysates. After incubation at 4 °C for 3 hr with gentle rotation, add 20 µl protein A/G magnetic beads (Pierce) each to the lysates and incubate another 2 hr at 4 °C with rotation. Wash the protein captured beads with NETN buffer 3 times for 5 min each at 4 °C with rotation. Then eluted beads with 50 µl 2×SDS loading buffer and the eluted protein or protein complexes could be detected by IB. The blotting signals were detected using Clarity Western ECL Substrate (Bio-Rad). As for peptide label tagged protein IP, the primary antibody and the protein A/G beads could be replaced with FLAG M2 magnetic beads (Sigma), S-protein agarose beads (Millipore), M-280 Streptavidin Dynabeads™ (Invitrogen) or HA magnetic beads (Pierce).

RNA Pulldown and Mass Spectrometry Analysis

RNA pull-down assay was performed as previously described with minor modifications^{16,30,54}. Biotin labeled RNA was generated using biotin-RNA labeling mix (Roche) and MEGAscript T7 or SP6 Transcription Kit (Thermo Fisher Scientific) and purified by RNA Clean & Concentrator-5 kit (Zymo Research). Cell lysate was prepared using polysome buffer (25 mM Tris-HCl pH7.5, 150 mM KCl, 0.5 mM

DTT, 0.5% NP-40) with complete protease inhibitor cocktail (Roche) and Ribolock RNase Inhibitor (Invitrogen). M-280 Streptavidin Dynabeads™ (Invitrogen) were prepared according to manufacturer's instructions and then incubated with 10 µg biotin labeled RNA (Sense and antisense separately) in RNA capture buffer (20 mM Tris-HCl pH 7.5, 1 M NaCl, and 1 mM EDTA) with RNase Inhibitor for 30 min at RT. Wash the RNA-captured beads once with NT2 buffer (50 mM Tris-HCl pH 7.4, 150 mM NaCl, 1 mM MgCl₂, 0.05% NP-40). Incubate the RNA captured beads and the non-RNA-captured beads control separately with prepared 30 mg cell lysates for 2 hr at 4 °C with gentle rotation. Then wash the beads with NT2 buffer three times, NT2 high salt buffer (NT2 buffer with 500 mM NaCl) twice, and PBS once for 5 min at 4 °C and finally add 50 µl 2×SDS-loading buffer 95 °C heat for 10 to 15 min. The product could be subject to MS analysis. As for western blot detection, 0.5-1mg cell lysate and 1-3 µg biotin-RNA would be sufficient. As for purified protein-RNA pulldown assay, 1-2 µg purified protein and 1-3 µg biotin-RNA would be sufficient.

RNA Immunoprecipitation, RNA Extraction and RT-qPCR Detection

The enrichment of the interested protein process was mostly similar to the protein IP indicated in **Cell Lysis, Immunoprecipitation and Immunoblotting** section with the modification that all the processes should be in RNase-free way, additional Ribolock RNase Inhibitor (Invitrogen) was required, the lysis buffer was transferred to polysome buffer and the wash buffer was transferred to NT2 buffer. Then, use the TRIzol reagent (Invitrogen) to extract the associated RNAs according to the manufacturer's instructions. Reverse transcription was performed using the iscript cDNA synthesis kit (Bio-Rad) and the abundance of target RNAs was detected by iTaq™ Universal SYBR Green Supermix qPCR kit (Bio-RAD) according to the manufacturer's instructions.

RNA FISH and IF

RNA Fluorescence in situ hybridization (FISH) was performed with a FISH kit (Ribobio Co.) according to the manufacturer's instruction with minor modifications. Briefly, cells with indicated treatment were fixed in 4% formaldehyde for 10 min followed by washing with PBS. The fixed cells were further dehydration through 70%, 90% and 100% ethanol. The air-dried cells were subjected to incubation with 40 nM FISH probe (Ribobio Co.) in hybridization buffer (100 mg/ml dextran sulfate, 10% formamide in 2×SSC) at 75 °C for 3 min. The hybridization was then performed at 37 °C for 8 hr to overnight. Then, the slide was washed twice with 2×SSC (0.3 M NaCl, 0.03 M Na₃Citrate, pH 7.0) at RT. The air-dried slide was mounted with Prolong Gold Antifade Reagent with DAPI for detection.

As for immunofluorescence (IF), cells were cultured in chamber slides overnight and fixed with 3.7% formaldehyde in PBS for 10 min at RT, followed by permeabilization with 0.5% Triton X-100 in PBS for 10 min. Cells were then blocked with 5% FBS in PBS for 30 min at RT, and incubated with the indicated primary antibody for 1 hr at RT, followed by incubation with Anti-rabbit (or Mouse) IgG (H+L), F(ab')₂ Fragment (Alexa Fluor® 594 or 488 Conjugate) from Abcam for 30 min at RT. Coverslips were mounted on

slides using anti-fade mounting medium with DAPI. IF images were acquired on a FV3000 confocal microscope (Olympus). For each channel, all images were acquired with the same settings.

***In vitro* Protein Pulldown Assay**

S-protein agarose beads (Millipore) or M-280 Streptavidin Dynabeads™ (Invitrogen) purified SFB (S-tag, FLAG, SBP) triple tagged protein was incubated with the NTR-Ni resin purified His-tagged protein 1-3 µg in 500 µl binding buffer (50 mM Tris-HCl pH 7.9, 10% Glycerol, 100 mM KCl, 5 mM MgCl₂, 10 mM β-ME, 0.1% NP-40) for 2 hr at 4 °C with gentle rotation. Then wash the beads with NETN buffer 3 times for 5 min each at 4 °C with rotation. Then eluted beads with 50 µl 2×SDS loading buffer and the eluted protein or protein complexes could be detected by IB.

***In vitro* MDH2 Enzyme Activity Assay**

Immunoprecipitated Flag-MDH2 protein was eluted using 3×Flag peptide. Then, 1 µg FLAG-MDH2 was added to 200 µl reaction buffer (0.2 mM oxaloacetic acid, 0.1 mM NADH in 1×PBS). The reaction speed was measured by detecting the decreasing absorbance at OD_{340 nm} in microplate system.

***In vitro* Deacetylation Assay**

Highly acetylated SFB-MDH2 protein was purified from SFB-MDH2 transduced HEK293T cells with TSA/NAM treatment using S-protein agarose beads (Millipore) or M-280 Streptavidin Dynabeads™ (Invitrogen). The reaction was performed in deacetylation buffer (40 mM HEPES pH 7.0, 6 mM MgCl₂, 1 mM NAD⁺, 1 mM DTT, and 10% glycerol) and 5 µg SFB-MDH2 and 5 µg MBP-His-SIRT3 were added together. The reaction should be conducted at 37 °C for 1 hr in a total volume of 100 µl with gentle rotation. The efficiency of deacetylation could be determined by Western Blot.

ATP/ADP Ratio Detection

ATP/ADP was detected using ADP/ATP Ratio Assay Kit (Sigma). The method was according to the manufacturer's instructions with minor modification. In brief, cells were seeded equally in the 96-well plate. Add 90 µl freshly prepared ATP reagent into each well and mix. Incubate plate for 1 min at RT and read the luminescence (relative light units) on a luminometer for the ATP assay (RLU_A). Then incubate the plate for another 10 min and add 6 µl ADP reagent. After 10 min incubation, read luminescence for ATP (RLU_B). Immediately add 5 µl ADP reagent and incubate 1 min. Read the luminescence (RLU_C). The ADP/ATP ratio was calculated as (RLU_C - RLU_B) / RLU_A.

As for mitochondrial ATP/ADP measurement, cells should be treated with recording buffer (5 mM 2-DG, 5 mM pyruvate, 156 mM NaCl, 3 mM MgSO₄, 2 mM KCl, 1.25 mM KH₂PO₄, 2 mM CaCl₂, 20 mM HEPES, pH7.35) 2 hr before measurement. The following steps were the same.

NADH/NAD⁺ Ratio Detection

NADH/NAD⁺ was detected using NAD/NADH-Glo™ Assay kit (Promega) in accordance to the manufacturer's instructions with minor modification. In brief, the cells were equally seeded in the 96-wells plate. When detection, cell culture medium should be removed and replaced with 50 µl PBS. Cells should be lysed by adding additional 50 µl base solution (0.2 M NaOH) with 1% DTAB to each well.

As for NAD⁺ detection, transfer 25 µl the indicated cell lysate to a new tube and add 25 µl 0.4M HCl and heat at 60 °C for 15 min. Incubate the sample at RT for 10 min and add 25 µl 0.5 M Trizma® base solution (Sigma). Add 50 µl freshly prepared NAD/NADH-Glo™ Detection Reagent to the sample to determine the NAD⁺ abundance by luciferase report in the microplate reader.

As for NADH detection, transfer 25 µl the indicated cell lysate to a new tube and heat at 60 °C for 15 min. Incubate the sample at RT for 10 min and add 50 µl HCl-Trizma® solution (0.4 M HCl, 0.5 M Trizma® base). Add 50 µl freshly prepared NAD/NADH-Glo™ Detection Reagent to the sample to determine the NADH abundance by luciferase report in the microplate reader.

Finally, the relative NADH/NAD⁺ was determined as the NADH abundance/ the NAD⁺ abundance ratio.

As for mitochondria NADH/NAD⁺ measurement, the mitochondria were quickly isolated according to **LMF, Mitochondria and Lysosome Purification** section and the following process was the same.

Malate and Citrate Assay

Intracellular citrate or malate was detected by Citrate or Malate Assay Kit (MAK067 and MAK057, Sigma) in accordance to the manufacturer's instructions with minor modification. Briefly, cells (~10⁶) were washed with ice-cold PBS and rapidly homogenized in 100 µl citrate or malate assay buffer. Samples were centrifuged at 15,000 g for 10 min at 4 °C to remove insoluble materials. Supernatants were filtered by 10 kDa MWCO spin filter (Millipore) and then assayed using the detection buffers in the kit. The measurement was performed using microplate reader at the specific wavelength according to the manufacturer's instructions.

Measurement of Cell Respiration

The oxygen consumption rate (OCR) was determined in cell extracts using Seahorse Bioscience XF-24 Extracellular Flux Analyzer. 10⁴ cells were seeded in XF24-well cell culture microplates (Seahorse Bioscience) for 24 hr. During respirometry, wells were sequentially injected at the indicated time points with 1.0 µM oligomycin (Oligo) to assess ATP turnover required respiration; 0.5 µM carbonyl cyanide p-[trifluoromethoxy]-phenyl-hydrazine (FCCP) to induce maximal respiration. Rotenone/Antimycin A was then added at a final concentration of 1.0 µM to inhibit electron transport and non-mitochondrial basal respiration level would be detected.

Colony Formation Assay

Equal numbers of cells were seeded in 6-well plate at a density of 500 cells each well. The cells were cultured for 10-15 days with 5% FBS added DMEM in cell incubation. Then fix cells using formalin and stain in crystal violet. The colonies were counted and the relative colony number was collected.

Xenograft Mouse Model

All animal experiments were performed according to the protocol approved by the Institutional Animal Care. Prepared tumor cells in 30 μ l sterile PBS were injected separately into the flank of five to six weeks old female nude mice, using the 100 μ l sterile syringe. The tumor size was measured every two days using a caliper, and tumor volume was calculated using the standard formula: $0.54 \times L \times W^2$, where the L referred to the longest diameter and the W referred to the shortest diameter. Mice were euthanized when they met the institutional euthanasia criteria for the tumor size and overall health condition. The solid tumors were removed, photographed and weighed.

Immunohistochemistry (IHC) Staining

The paraffin embedded tissues were deparaffinized in xylene followed by rehydration in a standard alcohol series, followed by antigen retrieval by 100 °C heating for 15 min in citrate buffer. The indicated primary antibody were diluted in 3% BSA and dropped to the tissue slides and incubated at 4 °C overnight. Simply wash the slides using PBS and incubate with 3% BSA diluted anti-rabbit or mouse HRP-secondary antibody for 60 min at RT. The slides were dehydrated in 50%, 70%, 80%, 95% and 100% ethanol, and stabilized with mounting medium. The images were acquired using Olympus BX43 microscope with Olympus cellSens Dimension software. The quantification of IHC staining density was measured using ImageJ software and calculated on the basis of the average staining intensity and the percentage of positively stained cells. A total score of protein abundance was calculated from both the percentage of positive cells and the intensity. High and low protein abundance was determined basing on the mean score of all samples as a cutoff line. Survival curves were plotted using the Kaplan-Meier method and compared by log-rank test.

QUANTIFICATION AND STATISTICAL ANALYSIS

The experiment was set up to use 3-5 samples/repeats per experiment/group/condition to detect a 2-fold difference with power of 80% and at the significance level of 0.05 by a two-sided test for significant studies. For immunohistochemical staining and immuno-blot, the representative images were shown. Each of these experiments was independently repeated for over 3 times. Relative quantities of gene expression level were normalized to *B2M* or *GAPDH*. Results were reported as mean \pm Standard Deviation (S.D.) of at least three independent experiments. Comparisons were performed using two tailed paired Student's *t*-test (* $P < 0.05$, ** $P < 0.01$, *** $P < 0.001$), as indicated in individual figures. For survival analysis, the expression of indicated genes was tested as a binary variant and divided into 'high' and 'low' groups. Kaplan-Meier survival curves were compared using the Gehan-Breslow test with Prism Software (GraphPad, La Jolla, CA). The experiments were not randomized. The investigators were not blinded to allocation during experiments and outcome assessment.

DATA AND SOFTWARE AVAILABILITY

All the sequencing data in this study have been deposited in the NCBI with accession number (BioProject: PRJNA594757). No data with mandated deposition. Source data for supporting the findings of this study are provided in the paper, and/or available from the corresponding author on reasonable request.

Figures

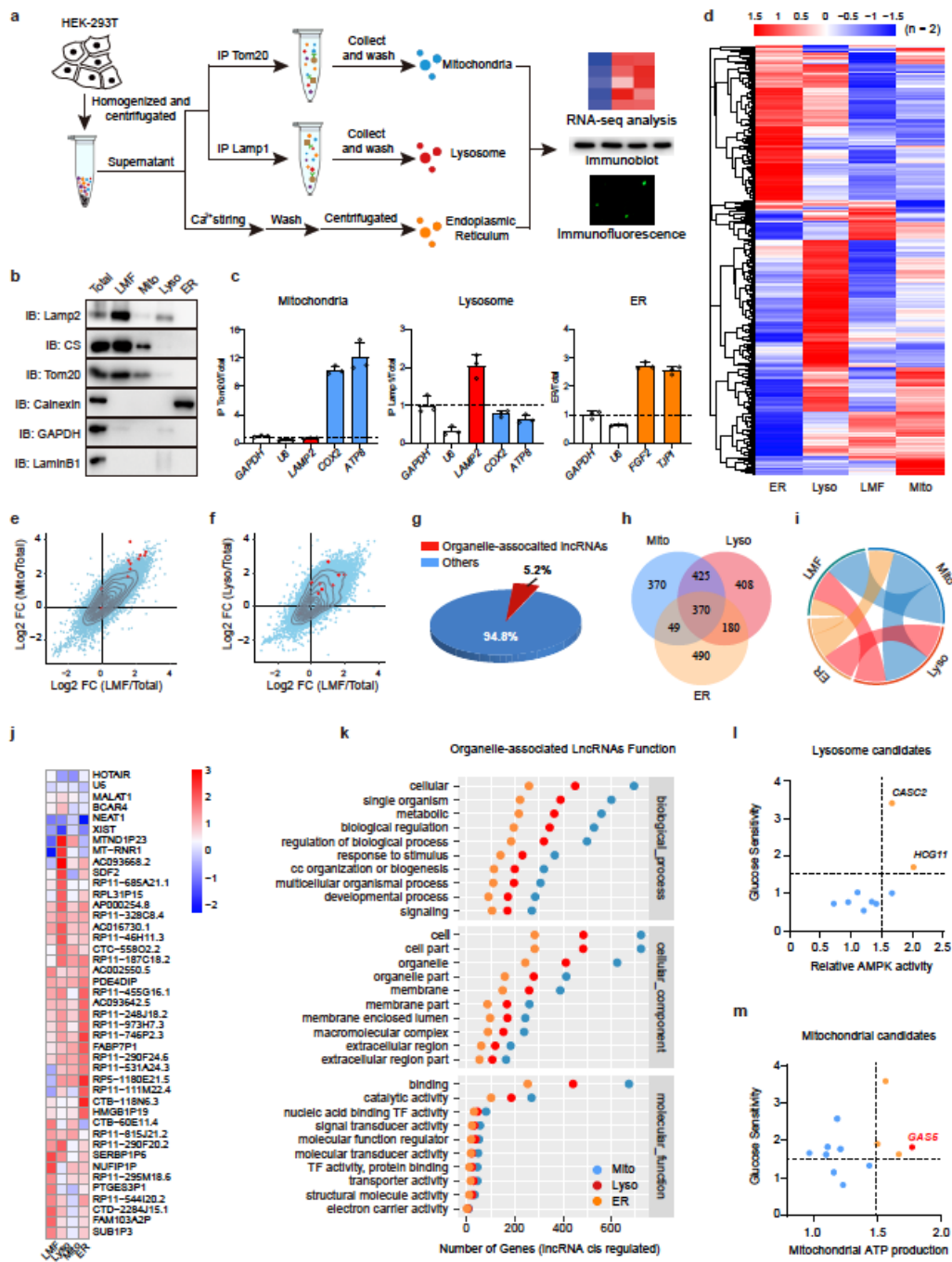


Fig. 1

Figure 1

The landscape of subcellular lncRNAs is established and qualified. (a) Experimental scheme for the establishment of the specific organelles' isolation process. The production could be used for RNA or protein detection. (b) Immunoblot (IB) detection of the purified organelles from HEK293T by the indicated protein markers to confirm the efficiency of the established organelles isolation method. Lamp2 for lysosome, CS and Tom20 for mitochondria, Calnexin for ER, GAPDH for cytosol and Lamin B1 for

nucleus. (c) RT-qPCR detection of the purified organelles (mitochondria in the left panel, lysosome in middle panel and ER in the right panel) from HEK293T by the indicated RNA markers to confirm the efficiency of the established organelles isolation method. U6 was used as nucleus marker, GAPDH was used as cytosol marker, LAMP2 was used as lysosome marker, COX2 and ATP8 were used as mitochondria marker, secreted protein genes FGF2 and TJP1 were used as ER marker. The relative enrichment of each RNAs was calculated by $2^{-(CtMito-CtTotal)}$ followed by normalizing all ratio value to the GAPDH in control group (the first GAPDH column). Cut-off line was thereby determined as 1. (d) Heatmap of enriched genes (the ratio of Total, fold change > 1.5, $P < 0.05$) in four groups. Each group contained two replicates ($n = 2$) and their mean value was used for heatmap. (e) Enrichment of MT-RNAs in mitochondrial compared with the crude light mitochondria fraction (LMF). All 13 mitochondria gene coded MT-RNAs (including CYB, ND6, ND5, ND4, ND4L, ND3, ND2, ND1, CO3, ATP6, ATP8, CO2, CO1) were shown in red points and 10 of them were enriched at a higher fold change in mitochondria than in LMF. (f) Enrichment of lysosome-associated RNAs compared with LMF. Potential lysosome markers (C12orf66, LAMP2, LAMP3, RAB7A, RHEBL1, RPS6KC1, SNX6, STX7, VPS26A) were shown in red points, and 8 of them were enriched at a higher fold change in lysosome than in LMF. (g) Organelle associated lncRNAs statistics. Criteria were enriched in at least one organelle, fold change > 1.5, $P < 0.05$. (h) Venn map for organelle associated lncRNAs. (i) Circos plot showing the co-localization of lncRNAs to multiple locations. (j) Heatmap of lncRNAs in subcellular organelles. Nucleus located RNAs (NEAT1/XIST/HOTAIR/MALAT1/U6) were shown as negative control. (k) The number of organelles-associated lncRNAs ($P > 0.05$, foldchange > 1.5) was calculated in each classified GO terms. lncRNAs' function was determined by the function of in cis associated neighbor genes (upstream or downstream 100K from lncRNA genome location). CC: cell component; TF: transcription factor. (l) Mitochondria were isolated and the glucose sensitivity index of mitochondria candidates was determined by RT-qPCR detection of mitochondria fraction under 8-hour glucose starvation or not. The mitochondrial ATP production index was determined by ATP/ADP detection under recording buffer treatment. Functional lncRNA candidates (both indexes' fold change > 1.5) were marked in orange and the most promising one was highlighted in red. (m) Lysosome was isolated and the glucose sensitivity index of lysosome candidates was determined by RT-qPCR detection of lysosome fraction under 2-hour glucose starvation or not. The relative AMPK activation index was determined by p-AMPK/AMPK ratio shown in IB detection (Extended Data Fig. 2f). Functional lncRNA candidates (both indexes' foldchange > 1.5) were marked in orange.

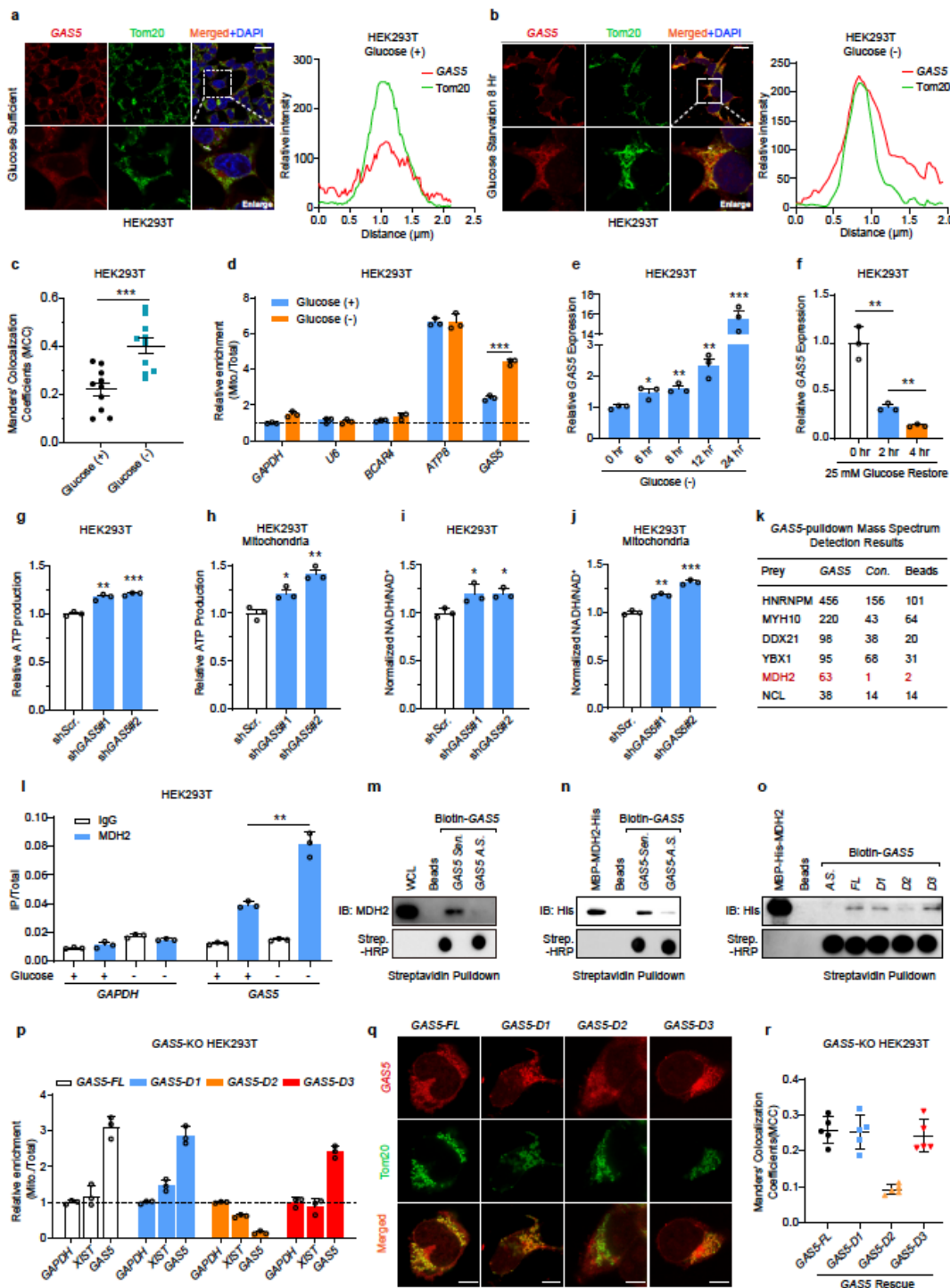


Fig. 2

Figure 2

Mitochondria associated lncRNA GAS5 is identified and characterized. (a-b) GAS5 FISH assay was performed in HEK293T under proficient (a) or deficient (b) glucose condition (Left panel). Line scan of the relative fluorescence intensity of the signal indicated as the dotted line in the left panel was plotted to show the peak overlapping (Right panel). GAS5 probe was labeled with Cy3 and mitochondria marker Tom20 was stained by Alexfluor488. Scale bar, 20 μm. (c) The percentage of mitochondria-colocalized

GAS5 per HEK293T cell under glucose sufficiency and deficiency was revealed by Manders' Colocalization Coefficients (MCC) between GAS5 (Cy3 red) and Tom20 (Alexfluor488 green), corresponding to GAS5-Tom20 fluorescence images (a-b). MCC was calculated as the light intensity of Tom20-colocalized GAS5 divided by the light intensity of total GAS5. (d) RT-qPCR detection of GAS5, U6 (nucleus marker), BCAR4 (nucleus lncRNA), GAPDH (cytosol marker) and ATP8 (mitochondria positive control) relative enrichment in isolated mitochondria from HEK293T under 8-hour glucose starvation or not. The relative enrichment of each RNAs was calculated by $2^{-(\text{CtMito}-\text{CtTotal})}$ followed by normalizing all ratio value to the GAPDH in control group (Value of the first GAPDH column was normalized as 1). Cut-off line was thereby determined as 1. (mean \pm S.D., n = 3 biological replicates, Student's t-test, ***P < 0.001). (e) RT-qPCR detection of GAS5 expression in HEK293T cells under glucose starvation with indicated time points. (mean \pm S.D., n = 3 biological replicates, Student's t-test, *P < 0.05, **P < 0.01, ***P < 0.001). (f) HEK293T cells were pretreated by 12-hour glucose starvation, and restored using 25 mM glucose DMEM culture for 2 or 4 hours. The expression of GAS5 in the indicated time points was detected by RT-qPCR. (g) Cellular ATP production was detected in HEK293T with Scramble or GAS5 knockdown (mean \pm S.D., n = 3 biological replicates, Student's t-test, **P < 0.01, ***P < 0.001). (h) Mitochondrial ATP production was detected in Scramble or GAS5 knocked down HEK293T with recording buffer treatment (mean \pm S.D., n = 3 biological replicates, Student's t-test, **P < 0.01, ***P < 0.001). (i) Cellular NADH/NAD⁺ ratio was determined in HEK293T (mean \pm S.D., n = 3 biological replicates, Student's t-test, *P < 0.05). (j) Mitochondria were isolated from HEK293T and mitochondrial NADH/NAD⁺ ratio was determined using isolated mitochondria (mean \pm S.D., n = 3 biological replicates, Student's t-test, **P < 0.01, ***P < 0.001). (k) Biotin-GAS5 was in vitro transcribed and used for HEK293T cell lysate RNA-pulldown assay, followed by mass spectrum analysis to explore the GAS5-binding proteins. The representative candidates were listed and the mitochondrial protein MDH2 was identified. (l) Endogenous RNA immunoprecipitation (RIP) assay was performed using IgG and MDH2 antibody in HEK293T cells, under 8-hour glucose starvation or not (mean \pm S.D., n = 3 biological replicates, Student's t-test, **P < 0.01). (m) In vitro transcribed biotinylated GAS5 sense (Sen.) or antisense (A.S.) transcripts were incubated with HEK293T lysate for RNA pulldown assay, followed by IB detection using the indicated antibodies. The input of biotin-RNAs was detected by dot blot using streptavidin-HRP. (n) IB confirmation of the GAS5-binding protein by in vitro-transcribed biotinylated GAS5 sense (Sen.) or antisense (A.S.) transcripts with bacterial purified MBP-His-MDH2. The input of biotin-RNAs was detected by dot blot using streptavidin-HRP. (o) IB detection of His-MBP-MDH2 protein retrieved by in vitro-transcribed biotinylated full-length and region partially deleted mutant (D1, D2, D3) GAS5. The input of biotin-RNAs was detected by dot blot using streptavidin-HRP. (p) RT-qPCR detection of GAS5, XIST (nucleus lncRNA) and GAPDH (cytosol marker) relative enrichment in isolated mitochondria from GAS5 and its mutants (GAS5-D1, D2, D3) rescued HEK293T GAS5-KO cells. The relative enrichment of each RNAs was calculated by $2^{-(\text{CtMito}-\text{CtTotal})}$ followed by normalizing all ratio value to the GAPDH in control group (the first GAPDH column of each rescued group was normalized as 1, separately). Cut-off line was thereby determined as 1. (q) RNA FISH detection of GAS5 in GAS5 and its mutants (GAS5-D1, D2, D3) rescued HEK293T GAS5-KO cells. Mitochondria was marked using Tom20 and Alexfluor488. Scale bar, 5 μ m. (r) GAS5-knockout HEK293T cells were transduced with GAS5-FL, D1, D2 and D3. The percentage of mitochondria-colocalized GAS5

per HEK293T was determined by Manders' Colocalization Coefficients (MCC) between GAS5 (Cy3 red) and Tom20 (Alexfluor488 green) from GAS5-Tom20 fluorescence images. MCC was calculated as the light intensity of Tom20-colocalized GAS5 divided by the light intensity of total GAS5.

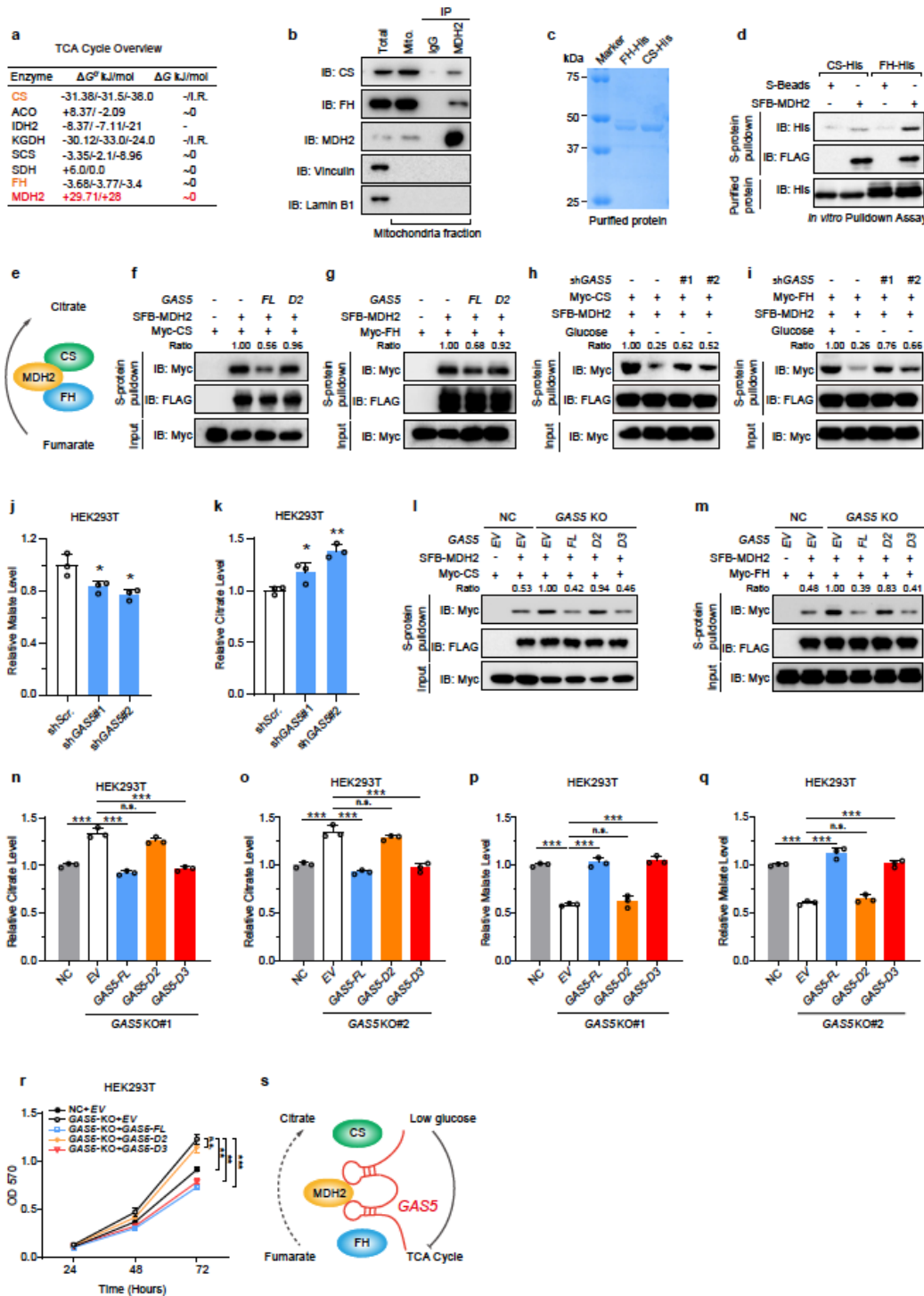


Fig. 3

Figure 3

GAS5 regulates the FH-MDH2-CS tandem association to modulate mitochondrial metabolism. (a) Overview of the standard reaction Gibbs free energy (ΔG°) and in vivo ΔG of mitochondrial TCA cycle

steps was shown. I.R. means an irreversible reaction. The enzymes corresponding to each step were listed: citrate synthase (CS), aconitase (ACO), isocitrate dehydrogenase (IDH2), α -ketoglutarate dehydrogenase (KGDH), succinyl-CoA synthetase (SCS), succinate dehydrogenase (SDH), fumarase (FH), malate dehydrogenase (MDH2). Potentially associated ones were highlighted. (b) Mitochondria were isolated from HEK293T cells. Endogenous co-IP assay using IgG and MDH2 antibody was performed in isolated mitochondria fraction to detect MDH2-CS and MDH2-FH interaction. (c) The Coomassie staining gel of purified His-CS and His-FH was shown. (d) SFB-MDH2 was purified from HEK293T cells using S-protein beads (S-beads). In vitro pulldown assay was performed by incubating SFB-MDH2 captured S-beads with purified His-CS or FH protein. IB detection using indicated antibodies was shown. (e) The graphic illustration of the FH-MDH2-CS association with rapid fumarate-malate-oxaloacetate-citrate streaming. (f-g) SFB-MDH2 and Myc-CS (f) or Myc-FH (g) were co-overexpressed in GAS5-FL or GAS5-D2 overexpressed HEK293T. Co-immunoprecipitation (Co-IP) assay was performed to detect the MDH2-CS (f) and MDH2-FH (g) interaction. (h-i) SFB-MDH2 and Myc-CS (h) or Myc-FH (i) were co-overexpressed in Scramble control or GAS5 knocked down HEK293T. Co-IP assay was performed to detect the MDH2-CS (h) or MDH2-FH (i) interaction with 8-hour glucose starvation or not. (j-k) Cellular malate (j) and citrate (k) were detected in Scramble or GAS5 knocked down HEK293T cells. Data are mean \pm S.D.; n = 3 per group. Student's t-test, *P < 0.05, **P < 0.01. (l-m) HEK293T GAS5-KO cells were rescued by GAS5-FL and its mutants (GAS5-D2, D3). SFB-MDH2 and Myc-CS (l) or Myc-FH (m) were co-transduced in non-specific control (NC) or rescued GAS5-KO HEK293T. Co-IP assay was performed to detect the MDH2-CS (l) or MDH2-FH (m) interaction. (n-q) GAS5-KO, including clone #1 (n, p) and clone #2 (o, q), HEK293T was rescued by GAS5-FL, D2 and D3. Their cellular citrate (n, o) and malate level (p, q) were measured. Data are mean \pm S.D.; n = 3 per group. Student's t-test, ***P < 0.001. (r) GAS5-KO HEK293T was rescued by GAS5-FL, D2 and D3. Their cell growth viability was determined by MTT assay in the indicated time points. Data are mean \pm S.D.; n = 3 per group. Student's t-test, **P < 0.01, ***P < 0.001. (s) The graphic illustration of GAS5-mediated disassembly of FH-MDH2-CS association with the slow TCA metabolites streaming.

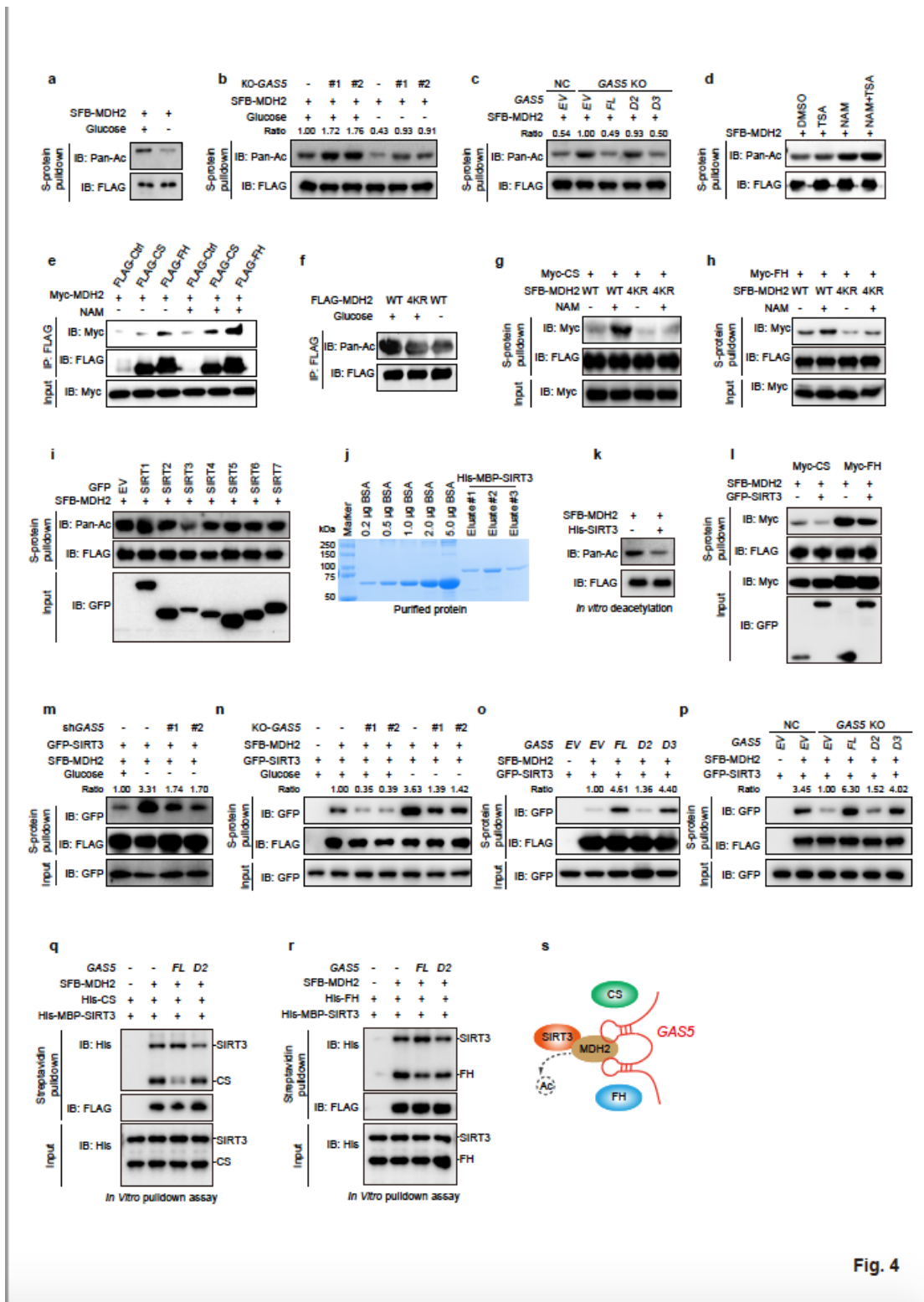


Fig. 4

Figure 4

GAS5 regulates FH-MDH2-CS association by declining MDH2 acetylation. (a) SFB-MDH2 was transduced in HEK293T cells, and was pulled down using S-protein beads. Immunoblot (IB) detection of the acetylation level of precipitated SFB-MDH2 under 8-hour glucose starvation or not used the Pan-Acetylation antibody. (b) IB detection of the transduced SFB-MDH2 acetylation level under 8-hour glucose starvation or not using Pan-Acetylation antibody, in GAS5 knockout HEK293T cells (clone #1 and clone

#2). (c) SFB-MDH2 was transduced in GAS5-FL, D2 or D3 rescued GAS5 KO HEK293T. SFB-MDH2 was pulled down by S-protein beads and the acetylation of MDH2 was detected using Pan-Acetylation antibody. (d) S-protein beads pulldown coupled Pan-acetylation antibody IB detection of transduced SFB-MDH2 acetylation level under Nicotinamide (NAM, an inhibitor of SIRT3) treatment with individual or additional Trichostatin A (TSA, an inhibitor of HDACs) treatment. (e) Myc-MDH2 and FLAG-CS or FLAG-FH were co-overexpressed in HEK293T. Co-IP detection of the MDH2-CS or MDH2-FH interaction with NAM treatment was performed using indicated antibodies. (f) FLAG-MDH2 wild type (WT) and 4KR (K185R, K301R, K307R, K314R) acetylation deficient mutant were overexpressed in HEK293T and the acetylation of FLAG-MDH2 WT and 4KR was detected by IP-IB using indicated antibodies. (g-h) SFB-MDH2 wild type (WT) or 4KR mutant were co-overexpressed with Myc-CS (g) or Myc-FH (h) in HEK293T. Co-IP detection of CS-MDH2 or FH-MDH2 association using indicated antibodies with NAM treatment. (i) S-protein beads pulldown followed by Pan-acetylation antibody IB detection of transduced SFB-MDH2 acetylation level by Pan-acetylation antibody with GFP-SIRT1-7 overexpression. (j) Coomassie staining gel of the purified His-MBP-SIRT3 protein, and the concentration was determined using the indicated BSA standards. (k) Highly Acetylated SFB-MDH2 protein was purified from NAM treated HEK293T cells using S-protein beads (S-beads). In vitro deacetylation assay was performed by incubating SFB-MDH2 captured S-beads with bacterial purified His-MBP-SIRT3 protein for reaction. The acetylation relapse of SFB-MDH2 was detected by IB using Pan-acetylation antibody. (l) GFP-SIRT3 and Myc-CS or FH were co-overexpressed in SFB-MDH2 transduced HEK293T. The interaction between MDH2 and CS or FH was determined by co-IP-IB using indicated antibodies. (m) SFB-MDH2 and GFP-SIRT3 were co-overexpressed in Scramble control or GAS5 knocked down HEK293T cells. Co-IP assay was performed using S-protein beads to detect the MDH2-SIRT3 interaction with 8-hour glucose starvation treatment. (n) SFB-MDH2 and GFP-SIRT3 was co-transduced in NC or GAS5-KO (clone #1 and clone #2) HEK293T cells and treated with sufficient or deficient glucose culture for 8 hours. SFB-MDH2 was pulled down by S-protein beads and co-precipitated GFP-SIRT3 was detected by GFP antibody immunoblot. (o) SFB-MDH2 and GFP-SIRT3 were co-transduced in GAS5 or its mutants (GAS5-D2, D3) overexpressed HEK293T cells. SFB-MDH2 was pulled down by S-protein beads and co-precipitated GFP-SIRT3 was detected by GFP antibody immunoblot. (p) SFB-MDH2 and GFP-SIRT3 were co-transduced in GAS5-FL, D2 or D3 rescued GAS5 KO HEK293T. SFB-MDH2 was pulled down by S-protein beads and co-precipitated GFP-SIRT3 was detected by GFP antibody immunoblot. (q-r) SFB-MDH2 was purified from HEK293T cells using Streptavidin beads. In vitro pulldown was performed by incubating SFB-MDH2-harboring streptavidin bead with purified His-CS (q) or FH (r) protein and additional equimolar full-length (FL) or deletion 2 (D2) GAS5. IB detection using indicated antibodies was shown. (s) The graphic illustration of the GAS5-SIRT3 regulated MDH2 deacetylation and CS-MDH2-FH disassembly.

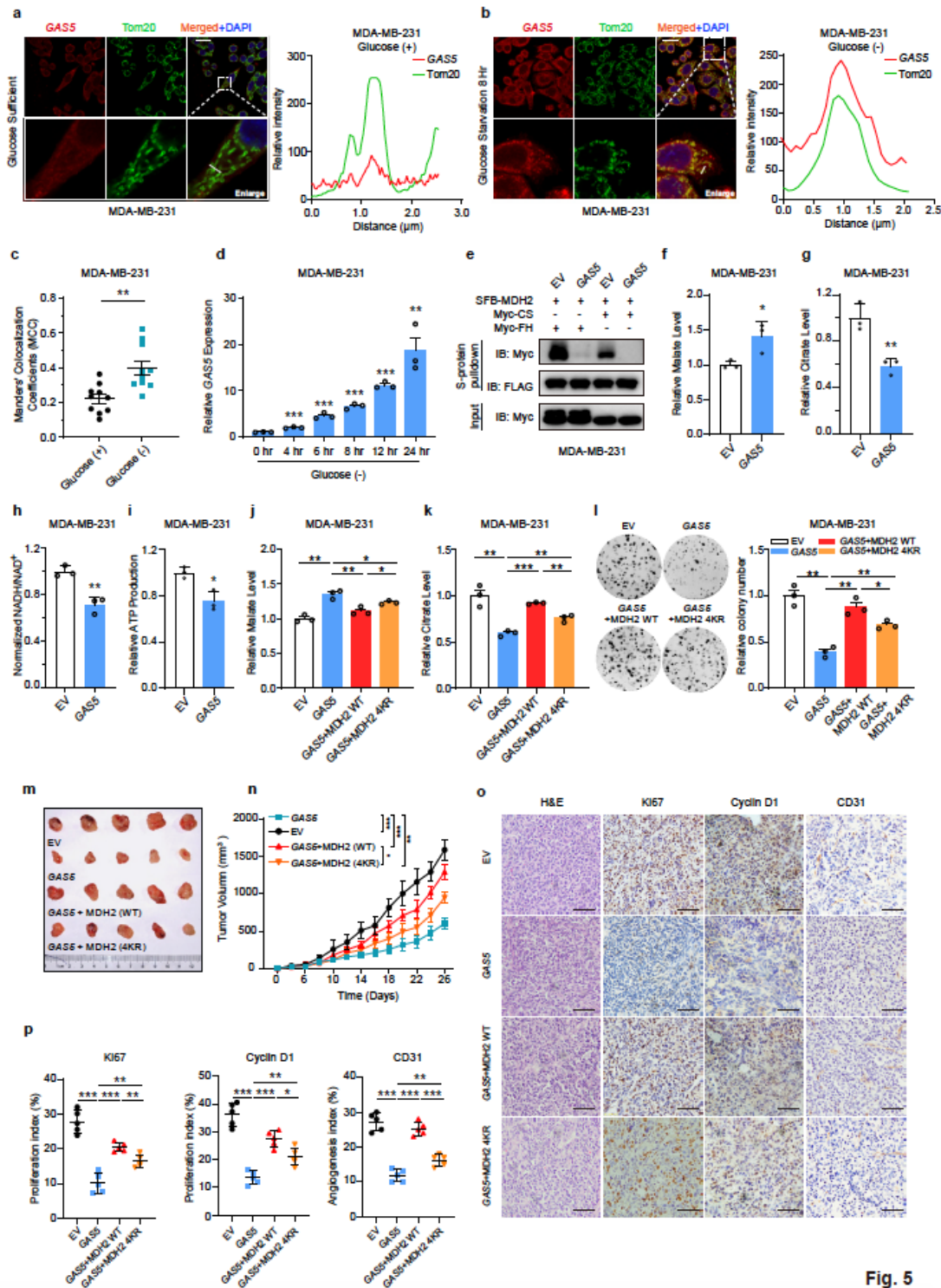


Fig. 5

Figure 5

Mitochondria-associated lncRNA GAS5 regulates TCA flux in tumorigenesis. (a-b) GAS5 FISH assay was performed in human breast cancer cell line MDA-MB-231, under proficient (a) or deficient (b) glucose condition (Left panel). Line scan of the relative fluorescence intensity of the signal indicated as the dotted line in the left panel was plotted to show the peak overlapping (Right panel). GAS5 probe was labeled with Cy3 and mitochondria marker Tom20 was stained by Alexfluor488. Scale bar, 20 μm. (c) The

percentage of mitochondria-colocalized GAS5 per MDA-MB-231 cell under glucose sufficiency and deficiency was revealed by Manders' Colocalization Coefficients (MCC) between GAS5 (Cy3 red) and Tom20 (Alexfluo488 green), corresponding to GAS5-Tom20 fluorescence images (a-b). MCC was calculated as the light intensity of Tom20-colocalized GAS5 divided by the light intensity of total GAS5. (d) RT-qPCR detection of GAS5 expression in MDA-MB-231 cells under glucose starvation with indicated time points. (mean \pm S.D., n = 3 biological replicates, Student's t-test, *P < 0.05, **P < 0.01, ***P < 0.001). (e) SFB-MDH2 and Myc-CS or Myc-FH were co-overexpressed in empty vector (EV) control or GAS5 overexpressed MDA-MB-231 cells. Co-immunoprecipitation (Co-IP) assay was performed to detect the MDH2-CS and MDH2-FH interaction. (f-g) Cellular malate (f) and citrate (g) levels were measured in empty vector (EV) control or GAS5 overexpressed MDA-MB-231 cells. Data are mean \pm S.D.; n = 3 per group. Student's t-test, *P < 0.05, **P < 0.01. (h) Cellular NADH/NAD⁺ ratio was detected in empty vector (EV) control or GAS5 overexpressed MDA-MB-231 cells with recording buffer treatment. Data are mean \pm S.D.; n = 3 per group. Student's t-test, **P < 0.01. (i) Cellular ATP generation was detected in empty vector (EV) control or GAS5 overexpressed MDA-MB-231 cells with recording buffer treatment. Data are mean \pm S.D.; n = 3 per group. Student's t-test, *P < 0.05. (j-k) Cellular malate (j) and citrate (k) levels were determined in empty vector control (EV), GAS5 individually, GAS5/MDH2-WT and GAS5/MDH2-4KR overexpressed MDA-MB-231 cells (Mean \pm S.D., n = 3 biological replicates, Student's t-test, *P < 0.05, **P < 0.01, ***P < 0.001). (l) Colony formation assay was performed in empty vector control (EV), GAS5 individually, GAS5/MDH2-WT and GAS5/MDH2-4KR overexpressed MDA-MB-231 cells (left panel). The statistical analysis was shown (right panel) (Mean \pm S.D., n = 3 biological replicates, Student's t-test, *P < 0.05, **P < 0.01). (m) Xenograft mouse model using empty vector (EV) control or GAS5 overexpressed MDA-MB-231 cells and ones with additional transduced MDH2 wild type (WT) or acetylation-deficient mutant (4KR). The in vivo generated tumors were shown. (n) In vivo analyses of tumors' growth and volume in xenograft mouse model were shown. Data are mean \pm S.D.; n = 5 mice per group. Student's t-test, *P < 0.05, **P < 0.01, ***P < 0.001. (o-p) Representative immunohistochemical staining (IHC) was performed in randomly selected tumors from mice that were subcutaneously injected with the indicated stably transduced MDA-MB-231 cells (o). Scale bar, 100 μ m. The relative intensities of immunohistochemical staining (p) were quantified by Image J software (mean \pm S.D., n = 5 biological replicates, Student's t-test, *P < 0.05, **P < 0.01, ***P < 0.001).

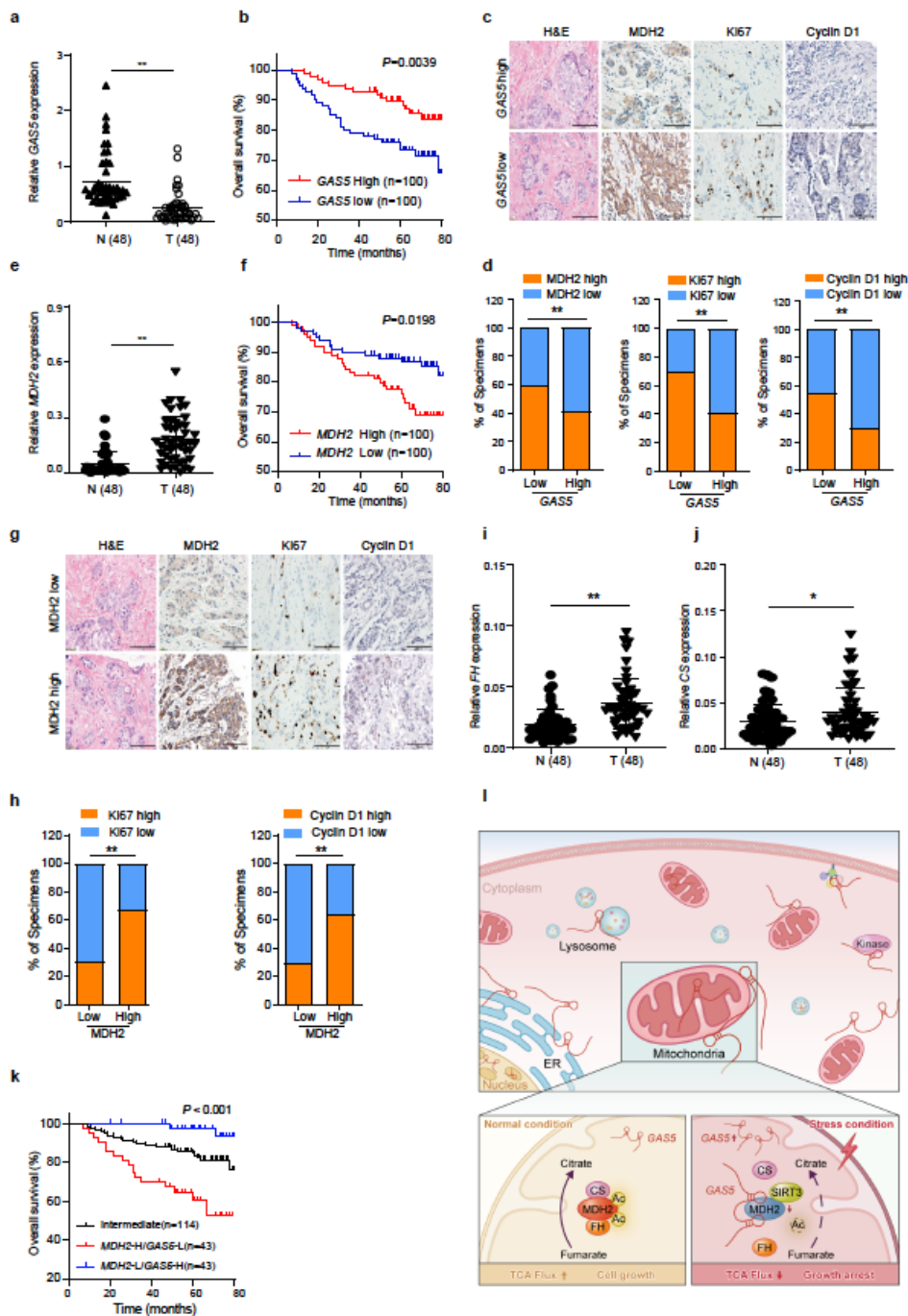


Fig. 6

Figure 6

High GAS5 expression and weak TCA sustaining benefit clinical outcomes in human cancer patients. (a) RT-qPCR detection of GAS5 expression in adjacent normal tissues (N) and malignant breast cancer (T) (SYSUCC Cohorts, Student's t-test, **P < 0.01). (b) Overall survival analysis of GAS5 status in breast cancer patients (SYSUCC Cohorts) detected by qRT-PCR (n = 200 patients, Gehan-Breslow test). (c) The expression of MDH2, Ki67 and Cyclin D1 in 100 primary human breast cancer specimens (SYSUCC

Cohorts, including GAS5-high and -low subsets) was detected by IHC assay. Scale bar, 100 μ m. (d) Percentages of specimens showing low or high GAS5 expression related to levels of MDH2, Ki67 and Cyclin D1 (Chi-square test, $**P < 0.01$). (e) RT-qPCR detection of MDH2 expression in adjacent normal tissues (N) and malignant breast cancer (T) (Sun Yat-sen Cohorts, Student's t-test, $**P < 0.01$). (f) Overall survival analysis of MDH2 status in breast cancer patients (SYSUCC Cohorts) detected by RT-qPCR (n = 200 patients, Gehan-Breslow test). (g) The expression of Ki67 and Cyclin D1 in 100 primary human breast cancer specimens (SYSUCC Cohorts, including MDH2-high and -low subsets) was detected by IHC assay. Scale bar, 100 μ m. (h) Percentages of specimens showing low or high MDH2 expression related to levels of Ki67 and Cyclin D1 (Chi-square test, $**P < 0.01$). (i-j) RT-qPCR detection of CS (i) or FH (j) expression in adjacent normal tissues (N) and malignant breast cancer (T) (SYSUCC Cohorts, Student's t-test, $**P < 0.01$). (k) Breast cancer patients (Sun Yat-sen Cohorts, n = 200) were divided into three groups according to expression scoring of GAS5 and MDH2, and the overall survival curve was generated with Kaplan-Meier analysis. (l) The graphic summary of subcellular RNAs' distribution and associated function, especially illustrating the mitochondria one.

Supplementary Files

This is a list of supplementary files associated with this preprint. Click to download.

- [Sangetal2020SupplementaryTable1.xlsx](#)
- [Sangetal2020SupplementaryTable2.xlsx](#)
- [Sangetal2020SupplementaryTable3.xlsx](#)
- [Sangetal2020SupplementaryTable4.xlsx](#)
- [Sangetal2020NewSupplementalFigure.pdf](#)
- [SUPPLEMENTARYFIGURELEGENDS.docx](#)